Final Technical Report

External Grant Award Number:
G12AP20026

Recipient:
Optim SDS

Principal Investigators:
Aasha Pancha
Optim SDS, 200 South Virginia Street, Suite 560, Reno, NV, 89501
Telephone (775) 236-5869 Fax:(775) 324-5662 aashap@optimsds.com
Satish Pullammanappallil
Optim SDS, 200 South Virginia Street, Suite 560, Reno, NV, 89501
Telephone.: (775) 236-5891 Fax:(775) 324-5662 satish@optimsoftware.com

Title:
Determination of 3D-velocitystructure across the deepest portion of the Reno-Area Basin

NEHRP Elements(s)
Element I: National and regional earthquake hazards assessments
Keywords: Site effects, Basin effects, Ground motions, Seismic Zonation, Engineering seismology

Start date: January 2012
End Date: December 2012

Research supported by the U.S. Geological Survey (USGS), Department of the Interior, under USGS award number **G12AP20026**. The views and conclusions contained in this document are those of the authors and should not be interpreted as necessarily representing the official policies, either expressed or implied, of the U.S. Government.

External Grant Award Number **G12AP20026**

Determination of 3D-velocitystructure across the deepest portion of the Reno-Area Basin

Aasha Pancha
Optim SDS, 200 South Virginia Street, Suite 560, Reno, NV, 89501
Telephone (775) 236-5869 Fax:(775) 324-5662 aashap@optimsds.com
Satish Pullammanappallil
Optim SDS, 200 South Virginia Street, Suite 560, Reno, NV, 89501
Telephone.: (775) 236-5891 Fax:(775) 324-5662 satish@optimsoftware.com

ABSTRACT

Estimation of shallow shear velocities is a key element in the assessment of sites for potential earthquake ground shaking and damage. We assess shear-wave velocities across the deepest portion of the Reno-area basin as defined by gravity. Little structural and velocity data is available for this section of the basin. To date, no permanent seismic instrumentation is located over this deepest portion of the basin. Existing velocity models for the region from regional earthquake analysis are limited in resolution to intervals of 1 km to 3 km. As a result, 3D basin details are currently insufficient for scenario modeling, an essential component of seismic hazard evaluation. Shear velocity to depths of up to 1000 m were measured using refraction-microtremor (ReMi) arrays across this portion of the basin with 50 m depth resolution. This was achieved through the deployment of standalone wireless instruments to record ambient urban noise. Two parallel arrays, each 5.8 km in length, and one orthogonal array 2.9 km long, were installed. Each array consisting of 30 wireless instruments, with the long ones having 200 m and short one 100m spacing respectively. The ReMi technique was employed to obtain 1D velocity profiles as a function of depth along each array from recorded ambient noise. To map depth and characterize lateral velocity heterogeneity beneath each array, subsets of 15 instruments were used to obtain a series of 1D velocity-depth profiles. These 1D velocity-depth profiles were then interpolated to obtain 2D and 3D structural representations of shear-wave velocities.

Our efforts in this project will allow characterization of the velocity structure beneath a region of the Reno-area basin which has the potential to produce strong ground shaking due to the sediments thickness in this locality. Efforts will contribute towards development of the Western Basin and Range Community Velocity model and the Reno-Carson City urban hazard map. As a result, ground-motion modeling capabilities will be improved contributing toward the goal of predicting earthquake ground motions in urban areas and other sensitive sites.

External Grant Award Number **G12AP20026**

Determination of 3D-velocitystructure across the deepest portion of the Reno-Area Basin

Aasha Pancha
Optim SDS, 200 South Virginia Street, Suite 560, Reno, NV, 89501
Telephone (775) 236-5869 Fax:(775) 324-5662 aashap@optimsds.com
Satish Pullammanappallil
Optim SDS, 200 South Virginia Street, Suite 560, Reno, NV, 89501
Telephone.: (775) 236-5891 Fax:(775) 324-5662 satish@optimsoftware.com

NEHRP Elements(s)
Element I: National and regional earthquake hazards assessments
Keywords: Site effects, Basin effects, Ground motions, Seismic zonation, Engineering seismology

1. Introduction

1.1 Objectives:

A key component of local seismic hazard assessment is the estimation or quantification of local site response. Current hazard estimates for the Reno area given by the U.S. Geological Survey National Hazard Maps are nominally appropriate for rock sites. This study contributes towards quantifying adjustments to account for local site and basin effects. The small basin size, compared to other urban basins like Los Angeles and Las Vegas, and the growing Advanced National Seismic System (ANSS) accelerograph network within it make this area a very attractive location for improving modeling techniques to explain the relationship between basin structure, near-surface geology, and ground motions. However, current velocity data for the Reno-area basin are limited in resolution to intervals of 1 km. As a result, 3D basin details are currently insufficient for ground motion simulation (Pancha *et al*., 2004). Such capabilities are essential for seismic hazard evaluation of densely populated urban regions. This project obtains shallow shear-velocity sections across the deepest section of the Reno-area basin.

At present, no permanent seismic station is located over the deepest portion of the Reno-area basin, resulting in poorly resolved estimates using conventional tomography and cross-correlation techniques, which utilize earthquake recordings. Gravity data indicate that basin sediments are thickest to the west with maximum basin depths of 600-1000 m (Abbott and Louie, 2000; Widmer, 2005; Widmer *et al.*, 2007). Assumptions regarding the density of material beneath this portion of the basin are based upon surface geology. These basin depth models are therefore not fully constrained and may be influenced by the presence of diatomite and lacustrine deposits, as confirmed by Cashman *et al*. (2012). The noisy urban setting, logistics, and high cost mean conventional reflection and refraction studies are impractical for

imaging to great depths. Use of wireless standalone instruments together with ambient noise analysis using the refraction microtremo (ReMi) technique permits inexpensive acquisition and processing of multiple long array data, allowing velocity characterization of these deep sediments.

1.2 Prior efforts to characterize velocity and basin structure in the Reno area

The cities of Reno and Sparks, Nevada, are located in a fault controlled basin that is about 13-km wide and 21-km long. The formal name for the area is the Central Truckee Meadows, referring to the geomorphic flat region of Quaternary deposits enclosed by the dashed line in Figure 1(a). The basin area delineated by gravity is shown in Figure 1(b) based on the work by Abbott and Louie (2000). We refer to it as the Reno-area basin after the largest city in the Reno–Sparks urban area, following Abbott and Louie (2000).

Basins along the Sierra Range front, which includes the Reno-area basin, are the result of active extension and dextral shear that has occurred in about the last 12 to 3 Ma years (Trexler *et al.*, 2000). The basin is flanked by the Carson Range of the Sierra Nevada Mountains on the west, Peavine Mountain to the north, and the Virginia Range to the east. Mesozoic metavolcanic rocks, Cretaceous granites and Tertiary volcanic rocks, including andesitic flows of the Kate Peak Formation comprise these mountain ranges (Bonham and Bingler, 1973; Bell and Garside, 1987) and form the bedrock base of the basin (Cashman *et al.*, 2012). The Reno-area basin is a fault-bounded graben, with range front fault zones along the western Sierra Nevada margin to the south and an inferred fault bounding the Virginia Range along the eastern side, as described by the United States Geological Survey Quaternary fault and fold database (http://earthquakes.usgs.gov/regional/qfaults). Many of the faults and their naming presented in this database are founded on mapping and structural inferences which date back to the 1970's by Bonham and Bingler (1973), and work conducted in the 1908's (Bell and Bonham, 1987; Bell and Garside, 1987; Bonham and Rogers, 1983). At this time, much of the interpretation focused on the prominent bounding normal faults and the west dipping sediments in the half graben to the south of Reno, with the belief that these major faults extended into the Reno-area basin. Many of the faults mapped within the southern region of the basin are termed the "Mt Rose Fault Zone", to signify the extension of the west range-bounding fault system (Bonham and Bingler, 1973; Bonham and Rodgers, 1983). Recent field mapping, however, reveals east-dipping sediments in the western Reno-area basin, which abut a major west-dipping normal fault at the center of the basin, the "Virginia Street" fault (Frary *et al.*, 2011;, Cashman *et al.*, 2012; Fary, 2012; Stephenson *et al*., 2012). Evidence shows that the "Virginia Street" fault was active during the deposition of gravels, which began 2.6 Ma, as well as during the Quaternary. These current findings suggest that an accommodation zone exists between the east dipping west-bounding normal faults south of the region and the west dipping east-bounding normal "Virginia Street" fault labeled in Figure 2. No evidence of a mountain front fault along the western margin of the basin is apparent from field observations or the topographic expression (Cashman *et al.*, 2012).

The deepest portion of the basin, located on the west side of the Truckee Meadows, is approximately 1.1 km, as estimated from an initial gravity data set modeled by Abbott & Louie

(2000) (Figure 1b). More recent gravity modeling of the region utilizes additional data and geological constraints (Widmer, 2005; Widmer *et al*., 2007; Cashman *et al.*, 2012) and suggests a maximum depth of approximately 700 m, and shows a complex faulted basin structure comprised of four sub-basins. A temporary deployment installed during the 2008 Mogul, Nevada earthquake swarm included stations above this gravity low. Average travel time residuals are highest over this portion of the Reno-area basin confirming that the basin is thickest in this locality (Dhar *et al*., 2009).

Detailed descriptions of the sedimentary fill are described by Trexler and Cashman (2012) and Cashman *et al.* (2012) and references therein. The Neogene "Sandstone of the Hunter Creek", as termed by Bingler (1975), is the main sedimentary unit and is highly variable in lithofacies and thickness (Trexler and Cashman, 2012). It consists of a coarse-grained basal section, medium-to-fine grained intermediate section, and an upper diatomaceous section. Volcanic debris, tuffs, and laharic deposits also exist, particularly in the lower section. The basal section consists of a boulder conglomerate with mean last size increasing towards the contact with the Tertiary volcanic. Conglomerates within the Sandstone of the Hunter Creek are volcanic in composition with granite only occurring at the base of the formation. The primarily lacustrine deposits of the formation consist of fresh water diatomaceous sediments interbedded with coarse sandstones, shales, and gravels from small rivers. No evidence suggests that the sediments of the formation were deposited in a lake that was linked to other Neogene basins in the region (Trexler and Cashman, 2012). The Sandstone of the Hunter Creek are deposited in a structural synclinal low created through the uplift of the Carson Range to the south and Peavine Mountain to the north, and plunges eastward recording uplift of the Sierra relative to the eastern margin of the Reno-area basin (Cashman *et al.*, 2012). Structural dip within the strata recorded the continued uplift of the Carson Range and Peavine Mountain.

Around 2.6 Ma, the Gravels of Reno, which represent the initiation of glacial outwash sedimentation, were deposited and postdate the Sandstone of the Hunter Creek. The deposits fill a deeply incused canyon associated with a rapid drop in base-level, and pre-dates the progressive eastward tilting of the Hunter Creek formation (Cashman *et al.*, 2012). Quaternary deposits consist of glacio-fluvial sands and gravel carried out by drainages from the Sierra Nevada Ranges, and form terraces ranging in age from ~2.5 Ma to less than 10 ka in age. Each terrace is associated with major glaciations events (Cashman *et al.*, 2012). This outwash material interfingers with locally derived coarse pediment and alluvial fan deposits. Recent Quaternary deposits consist of sediments carried by the Truckee River, which initiated flow through the area in mid- to late- Tertiary time (Bell *et al*., 1989).

These basin sediments have undergone faulting as documented by Cashman *et al.* (2012). Numerous smaller scale faults exist within the Reno basin, including a "horst and graben" fault structure as discussed by Widmer (2005) and observed by Bonham and Bingler (1973) and Bonham and Rogers (1983). Major faults contributing to seismic hazard in the region have previously been documented by dePolo *et al*. (1997). These basin faults are characterized and documented by the United States Geological Survey Quaternary fault and fold database (http://earthquakes.usgs.gov/regional/qfaults) (Adams and Sawyer, 1999a, 199b; Sawyer, 1999). Steep gravity gradients located in the central Reno area coincides with the location of the Mount Rose Fault Zone (Sawyer, 1999). In support of the Western Basin and Range Community

Velocity Model and the proposed Reno-Carson City Urban Hazard Maps, a high-resolution seismic reflection imaging study of the Reno-area basin has been conducted in a joint collaborative effort by the U. S. Geological Survey, the University of Nevada, Reno, and nees@UTexas, Austin. Two seismic profiles were acquired towards understanding the basin structure and fault locations in the area (Frary *et al.*, 2011; Frary 2012) as well as S-wave velocity information through analysis of ambient noise using the ReMi technique (Odum *et al*., 2011). Interpretation of the data revealed many previously mapped faults as well as additional newly-recognized faults. Prior to this work, no faults had been recognized in the Reno downtown area (Stephenson *et al*., 2012). Discovery of these new faults has drawn attention for the need to reexamine the faults within the Reno-Carson City urban corridor as potential earthquake sources, updating the work of dePolo *et al.* (1997). However, this new data does not traverse the thickest portion of the basin, the focus of this study.

Characterization of velocity within the Reno-area basin has been limited until present. Prior to 2000, only one seismic sensor was located within the basin. Installation of the current ANSS network (Figure 1) began in 1999 and was completed in 2003. Currently no permanent seismic station is located over the deepest portion of the basin as defined by gravity. In addition, the network as a whole records a limited number of events. On average there are only 4.0 M=3 events and 0.6 M=4 events that occur per year in this region (dePolo *et al*., 1997). Events recorded by these ANSS strong motion instruments are often characterized by low signal to noise ratios due to a lack of strong shaking (Pancha *et al.*, 2007b). Nevertheless, using over 10,000 events and seismic stations across the northern Nevada/California region, Preston and von Seggern (2007) obtain a 3-D P- and S-wave tomograhpic inversion for the greater Reno-Carson urban corridor with resolution from 3 to 10 km depth. This model therefore does not allow for detailed velocity resolution of the Reno area basin. Cross-correlation of ambient noise between local ANSS stations (Tibuleac *et al.*, 2009; 2011) within the Reno-area basin (Figure 1) allowed velocities to be determined across the basin. However, the currently available model is only resolved on a horizontal grid with 6 km spacing and an initial surface layer thickness of 1 km (Louie *et al*., 2010).

Efforts to characterize shallow shear-wave velocities throughout the Reno-area basin using the refraction microtremor (ReMi) technique (Louie, 2001) have been ongoing. A transect conducted along the Truckee River (Figure 1) measured 54 shallow shear-wave velocity profiles spaced 300 m apart (Scott *et al.*, 2005). The aim of the study was to obtain average shallow shear-wave values to 30 m depth (Vs30). A portion of this transect spans the deepest portion of the basin. Although data to 200 m depth are presented by Scott *et al*. (2005) along the transect length, data beyond 100 m depth is less constrained due to the array length. Additional measurements are archived at www.seismo.unr.edu/vs/archive. These include 21 measurements made by Clark *et al.* (2005) to investigate the potential of a local fault as a hydrological barrier. More recently, ANSS stations within the Reno-Carson urban corridor have been characterized (Pancha *et al.*, 2007a), including under USGS-NEHRP sponsorship (external grant award numbers G09AP0051 (Louie) and G11AP20022 (Optim SDS))

1.3 Basement Gravity Models for the Reno-area basin

Two basin depth models exist for the Reno-area basin, as discussed above. The initial model developed by Abbott and Louie (2000) uses 200 new gravity measurements acquired in the Reno-Carson urban corridor, combined with an existing data set (Hittelman *et al*., 1994). As both lithological and density data for the region were lacking for the Reno-area, Abbott and Louie used information from well logs in conjunction with an average regional density contrasts for the Basin and Range Province used by Blakely *et al*. (1998) and Jachens and Moring (1990). Of the 26 well logs utilized to constrain the model, only 12 penetrate the Kate Peak Andesite, and are all located in a similar location within the Moana Hot Springs geothermal region to the south. Density approximations are therefore the principle source of error in their model, with upper and lower limits of the sediment-basement density contrast resulting in a 50% depth error. Based on their bedrock and basin gravity maps, and their final basement depth models, Abbott and Louie infer an estimated depth uncertainty of 250 m. In addition, Abbott and Louie (2000) state that logged well in Reno shows Hunter Creek sandstones and diatomites extending through 20–90% of the section, with varying density throughout the formation.

While the basement model developed by Abbott and Louie (2000) is a valuable first order model to characterize the basin shape, due to the lack of density data, the model fails to constrain the location and geometry of the basin structures. Towards understanding of the hydrographic nature of the basin, Michael Widmer (Central Truckee Meadows Remediation District, Washoe County Department of Water Resources, Reno, Nevada) has expanded and improved upon the efforts of Abbott and Louie (Cashman *et al*., 2012; Widmer *et al*. 2007; Widmer, 2005). A more sophisticated and detailed sedimentary basin model for the Reno-area is developed through: 1) the addition of new gravity measurements; 2) the measurement of 169 rock densities to define average densities of for the nine geological units used in the model; 3) incorporation of geological constraints from surface observations, supplemented by borehole data; and 4) the acknowledgment that the gravity anomalies reflect density changes that are the result of localized faults, paleotopography, and lateral facies changes, in addition to changes in thickness of the basin fill (Cashman *et al.*, 2012).

As the focus of the study was to define the distribution and thickness of the Plicoene and Pleistocene sediments, Cashman *et al*. (2012) subdivide the Hunter Creek formation into four units each with its own unique density based on multiple field measurements. Further, the Reno Gravels and the Quaternary deposits were noted to be comparable in density and composition, so are modeled as the same unit. Individual density values also distinguish the Tertiary volcanics of the Kate Peak formation, as well as the Createaceous granite and Mesozoic metavolcanics

Modeling results successfully show that the deepest negative anomaly lows in west Reno correlate primarily to the presence of diatomite rather than prominent basement lows. The gravity modeling also demonstrates that the diatomite section does not continue down-dip to great depths beyond the extend of the current outcrop in west Reno (Widmer *et al.*, 2007; Cashman *et al*., 2012), but contributes greatly to the gravity low due to its density of 1.0-1.16 g/cm^3 or 1.08-1.46 g/cm^3 for dry and wet samples respectively. This termination of the diatomite deposit delineates the eastern margin of lacustrine environment as discussed by Cashman *et al*. (2012). This western sub-basin terminates at a prominent north-south gravity gradient, which

defines the location of the west dipping normal fault through the center of the valley, the Mount Rose Fault Zone (Sawyer, 1999). Gravity lows observed in other regions of the basin document the topographic relief of the unconformable surface beneath the Neogene deposits, and the faulting of the Neogene and younger sediments within the Reno-area basin.

2. Array Configuration and Data Acquisition:

Through this awarded project, wireless instruments recorded ambient urban noise along three arrays across the western portion of the Reno-area basin. These seismic profiles traverse the deepest portion of the Reno-area basin, as defined by gravity (Abbott and Louie, 2000; Widmer, 2005; Cashman *et al*., 2012). The objective of the array deployment was to obtain shear-wave velocity information up to 1000 m depth with a depth resolution of 50 m Two parallel arrays 5.8 km in length, and one orthogonal array 2.9 km long, were installed, as shown in Figure 2. The selected line locations best capture the maximum basin depth and the extent of the basin structure, based on the current gravity basin depth models.

Each array consisted of 30 wireless instruments, spaced 200 m or 100m apart. These standalone Sigma™ cableless acquisition systems manufactured by iSeis (Heath, 2011), shown in Figure 3, were paired to standard vertical geophones with natural frequency of 4Hz. Each seismometer unit location was surveyed using a TopCon GRS-1 mobile handheld unit. Collected spatial data was then exported into a GIS format. Once deployed, and powered on, the Sigma™ units started recording passive data. Each Sigma™ unit has its own built in memory, so data is stored on each Sigma™ unit independently. As only 30 instruments were available, the three arrays could not be deployed simultaneously. Instead, each line was installed individually on three consecutive days during July, 2012. Each array was deployed for a total time length of two hours, at a sampling rate of 2 milliseconds. Once completion of recording each day, the data was downloaded from each unit and concatenated into single one-minute time records for each individual line.

Ability of the seismic array to image velocity structure at depth depends on the capability of the array to capture ground motion at wavelengths that sample the target depths. The frequency content of the recorded data is dependent on several factors. These include the array length, geophone spacing, sampling rate, geophone frequency, the time length of the data records, and the frequency content of the excited noise sources producing the recorded ground motions. Typically, the depth of penetration of the recorded wave field is half the array length. To successfully image the velocity profile of the entire sediment package and define the basin depth, the arrays presented in Figure 2 were intentionally 5.8 km and 2.9 km in length to ensure detection of the bedrock bottom, and characterize the changes in basin structure across the study region. With only 30 seismic available seismic recorders, the selected geophone spacing enabled suitable spatial coverage of the target region with sufficient sampling of low frequency waves to characterize the deep structure and maintain 50 m resolution. As discussed in the following analysis section, we investigated the appropriate time length of the recorded ambient noise required to successfully image Rayleigh-wave dispersion at low frequencies representative of the velocity structure at depth.

Use of wireless stand-alone instruments together with ambient noise enabled several long array data to be inexpensively acquired, with limited manpower. However, the urban environment necessitated the need for constant security monitoring of the instruments throughout the deployment, placing constraints on the maximum time span of recording due to budget restrictions.

3. Dispersion curve analysis and Shear-Wave Velocity Modeling:

The Refraction Microtremor (ReMi) (SeisOpt® ReMi™, ©Optim 2001-2012) method was used to obtain a series of 1D velocity profiles as function a of depth from the noise records captured by the three array lines shown in Figure 2. To map depth and characterize lateral velocity heterogeneity beneath each array, subsets of 15 instruments were used to obtain a series of 1D velocity-depth profiles. These 1D velocity-depth profiles were interpolated to obtain 2D and 3D structural representations of shear-wave velocities. Refraction microtremor is a volume-averaging surface-wave measurement, averaging velocities where geology is laterally variable, thus differing from single point data obtained from downhole logs. In this method, microtremor noise from sources such as traffic and freeways excites Rayleigh waves, are recorded by a linear array of vertical refraction geophones. The noise records are transformed into slowness–frequency (p-f) space, and a dispersion curve is picked along a minimum-velocity envelope where the gradient of the power spectral ratio is greatest (Louie, 2001; Pancha *et al*., 2008). Modeling of the dispersion curve produces a depth–velocity sounding (Figure 4, top), which can be vertically averaged to the single Vs30 value used by the NEHRP-UBC code.

To aid as reference models, velocity profiles were initially determined through the analysis of all 30 instruments located along each array. These reference models helped to constrain the average depth of the bedrock layer, and therefore restricting the shallower velocity structure and average velocity values for prominent geological interfaces. The maximum velocity of the bedrock basement was constrained to values consistent with the deeper velocity structure obtained by Preston and von Seggern (2007) through 3-D P- and S-wave tomograhpic inversion. These reference models are an average representation of the velocity structure along the entire length of each array.

In addition to array length and geophone spacing discussed previously, increasing the time length of the recorded noise also enables enhanced resolution of the low frequency energy of the recorded ambient noise. Louie's (2001) recommendation of 30 seconds data length was specified as guidelines for the determination of average velocities to 100m depth, the requirement for NEHRP-UBC code engineering assessment, the focus of that paper. In order to characterize deeper velocity structure, longer time records obviously are required. In the development of the velocity-depth soundings for each 30-instrument arrays, record lengths of 60 seconds were initially analyzed. This is the default output of the acquisition system. However, for all three lines, it was noted that, although dispersive energy was evident in these time records, this dispersive energy was more prominent when 120 second record lengths were utilized, particularly at low frequencies. Longer wavelength surface-wave data, recorded by the array configuration, sample deeper into the geologic structure. Naturally longer time intervals are

therefore required to capture their motion. This difference in clarity of the dispersive energy between 1-minute and 2-mintue record sections is demonstrated in Figure 5 for Line 3. While the one-minute records do characterize the dispersive energy at all frequencies, the energy is less distinguishable at very low frequencies. These low frequencies are highly visible using the two minute records. In the one minute records, the energy is only observed at certain frequencies for each record. However, energy is observed at all frequencies from the two minute records. A natural assumption would be that longer intervals would further enhance the clarity of the dispersive energy. However, as the array configuration was designed to capture surface-wave energy with wavelengths necessary for the determination of shear velocity structure to depths of at least 500 m basin with 50 m depth resolution. Wavelengths at periods which sample the shallow structure below 50 m depth are therefore poorly characterized. Closer geophone spacing is required to characterize the velocity structure in the upper 50 m.

To characterize and map the lateral velocity heterogeneity beneath the area, a series of 1D velocity-depth soundings were determined along each of the three array lines using subsets of instruments along each array. Each of these 1D soundings were then interpolated to obtain a 2D structural representation of shear-wave velocities such as that illustrated in Figure 5 (bottom). In essence, the 2D image is comprised from a moving array of instruments. Subsets of 15 consecutive geophone instruments used to produce a single 1D shear-wave velocity depth profile characterizing average the shallow structure beneath each subset of instruments. These “sub-arrays” were spaced along each array, nominally moving five instruments along each line. Where significant changes in the 1D velocity profiles were noted, additional sub-arrays were analyzed to adequate characterize structural changes along the length of each line. Table 1 lists the instrument subsets used to obtain 1D velocity soundings along each array. The microtremor data for each sub-array was wavefield-transformed to slowness-frequency space. Rayleigh-wave dispersion of the surface-wave was identified in slowness-frequency space, and a fundamental mode dispersion curve was picked. The dispersion curve was then forward modeled producing a shear-velocity-*vs.*-depth profile for each sub-array.

Modeling of subsets along each line was initially constrained using velocities from the reference model for the arrays as a guide. Velocity profiles obtained using all instruments along Lines 1, 2, and 3 were also used as reference guide. Velocity models for adjacent sub-arrays along each line were adjusted so that while layer velocities remained relatively unchanged, interface depths were modified. Small adjustments of the layer velocities and the introduction of additional layer interface were introduced to help match the dispersion curve data. The restriction of layer velocities enhanced the ability to map lateral changes in the velocity structure along each line, and to interpolate these changes across the study area to the adjacent array lines. Care was taken to ensure that the models obtained for sub-arrays along Lines 2 and 3 were in relative agreement with the intersecting sub-array models obtained along Line 1.

The preferred profile will always be the profile interpretation that results in the minimum number of layers to accommodate the observed Rayleigh-wave dispersion and produces a best estimate, reliable and repeatable velocity structure. Because forward modeling is used rather that an inverse method to obtain our velocity-depth model, we are able to test the necessity and sensitivity of the data to both layer thickness and layer velocity. The resultant model is therefore the simplest to explain the data. This follows from Occam's razor principle that "entities must

not be multiplied beyond necessity", that simply states, “one should not increase, beyond what is necessary, the number of entities required to explain anything”. Over-parameterization of the profile with too many layers complicated the detection of lateral changes in the structure along each array, defeating the purpose of characterizing notable geological features beneath the array.

4. Results

The 2D structural representation of the shear-velocities via these 1D soundings along Lines 1, 2 and 3 are presented in Figures 9, 10, and 11 respectively. These 2D images are compiled through interpolation of the 1D shear-velocity profiles as function of depth determined from the moving sub-array of instruments along each line length. Maximum depth resolution of each 1D profile, estimated using the approximation proposed by Park *et al*. (1999), was deeper than the depth to the basin basement determined for that location. For all three lines, material with shear-wave velocity of 2200 m /s defines the basement of the basin. Example of the p-f plots and dispersion of the Rayleigh wave energy are shown in Figures 6, 7, and 8 for Lines 1, 2, and 3 respectively along, with the resultant velocity-depth models.

Along the length of Line 1, the basement varies in from 240 m to 600 m depth (Figure 9). Eastward tilting of the sedimentary section observed by Cashman *et al.* (2012) and Stephenson *et al*. (2012) is evident in the eastern half of Line 1, between Station 15 and 23. Basement depth varies from 240 m at Station 18 to 420 m at Station 23, with some variation between, giving 6°-7° slope to the sediment package, which differs from the 23° tilt of the Tertiary section observed by Cashman *et al.* (2012). This 6°-7° slope in however in agreement with the 6°-8° eastward fault controlled dip observed by Stephenson *et al.* (2012) in seismic reflection sections. A deep basin low is observed between Station 11 and Station 13, which coincides with the locality of a dipping 200 m thick diatomite deposit reported by Cashman *et al.* Extension of this surface diatomite deposit by Cashman *et al.* to depth was require to match the observed gravity low. As the station spacing of the instruments in this study along Lines 1 and 3 is of the same order as the thickness of this deposit these low velocity diatomite sediments were undetected. Therefore, this basin low is more likely to be an expression of the bedrock paleotopography, reflecting the 3D geometry of the topographic high to the south of Stations 13 thorough 15 (Figure 2).

Variation in depth to bedrock observed along Line 2 is greater, with basement depths ranging from approximately 1100m in the north to 540 m in the south. This basement low, matches the location of the gravity low presented by Cashman *et al.* immediately to the south of the River and east of the McCarran Boulevard (Figure 2). As seen in Figure 10, a dramatic change in basement elevation takes place between Station 10 and 13. This change is located just north of a mid-late Quaternary fault, shown in green in Figure 2. Based on the interpretation of the 2D velocity representation shown in Figure 10, this change in basement level does not appear to be due to faulting. The sediment thicknesses on either side of the change are not equivalent. Instead, they taper in thickness towards the south, indicative of on-lapping of sediments towards the south. The fault documented by the United States Geological Survey Quaternary fault and fold database originated from the work of Bonham and Bingler (1973). Small topographic changes in relief noted along the length of this proposed fault in many places indicate the location of a terrace riser. Bonham and Bingler (1973) most likely misidentified the elevation

along feature as being the result of fault movement. We interpret the variation in basement elevation observed along Line 2 as an expression of the paleotopography related to river terraces cut by the Truckee River since 10Ma.

Bedrock basement slowly increases from west to east to the north along Line 3 from 720 m depth to 850 m (Figure 11). This progressive thickening is consistent with the location of the gravity low reported by Cashman *et al.* (2012). Although diatomite is observed at the surface along this array between Stations 10 and 13, as mentioned above, this deposit is only 200 m in thickness (Cashman *et al.*, 2012) and therefore, due to the 200 m instrument spacing along this line, is undetectable. Short station spacing, and sub-arrays shorter than the deposit thickness are required to characterize these low velocity sediments in the region.

5. Contribution towards Seismic Hazard Assessment and Ground motion prediction

Results of this study provide a more thorough characterization of basin structure. The basin depth and shear-wave velocity models presented above help identify areas susceptible to shaking during large earthquake events due to near-surface shear-wave velocity and basin depth. This effort contributes towards development of the Western Basin and Range Community Velocity model and the Reno-Carson City urban hazard map. The final step will be the incorporation of the shear-wave velocity structure into the Nevada ShakeZoning community seismic modeling environment at the Nevada Seismological Laboratory at the University of Nevada, Reno. This will aid improvement in ground-motion modeling capabilities contributing toward the goal of predicting earthquake ground motions in this highly populated and earthquake prone urban region.

Towards assisting development and implementation of the next generation attenuation (NGA) models, using the 1D velocity sounding along each site, values of average velocities Vs10, Vs30, Vs50 and Vs100 to depths of 10, 30, 50, and 100 meters are computed by arithmetic slowness averaging with the formula below:

$$VsZ = \frac{Z}{\sum_{1}^{N} \frac{z_i}{V_i}}$$

where Z is the total depth, z_i is the thickness of layer i with shear velocity V_i. Similarly, we have picked Z0.5, Z1.0, Z1.5, and Z2.0, which are the depths where the shear velocity first exceeds 0.5 km/s, 1.0 km/s, 1.5 km/s, and 2.0 km/s respectively. These values are listed in Table 1(a)-(c). Caution however must be used when using the Vs10 and Vs30 reported in Table 1(a)-(c). The large station spacing means that velocities above 50 m depth are not well resolved. To obtain reliable velocity estimates using ReMi in this depth range, additional arrays with closer station spacing are required. The shorter array lengths allow denser measurements to characterize the near-surface, which likely exhibits greater velocity variations.

6. 3D Shear-Wave Velocity representation:

Data from the 2D velocity representations for each of the three lines were interpolated to produce a 3D velocity volume over the area covered by the midpoints of the sub-arrays, as illustrated in Figure 12(a). Station locations transformed into co-ordinates relative into a common location to enabled the data to be mapped using the unit measure of meters. Slices through this volume in depth, the east-west direction (X) and the north-south direction (Y) are shown in Appendices A1.1 to A1.25, Appendices A2.1 to A2.4, and Appendices A3.1 to A3.5 respectively. The data interpolation was performed using SeisOpt®Vis3D™ (© Opim, Inc., 2008-2012), which uses a nearest-neighbor approach in addition to lateral smoothing. Away from the array locations, the velocity data extrapolates to lower values towards the edges of the volume. This is evident from the example given in Figure 12(b). As a result, areas of the volume not occupied by data points are not valid interpretations of the velocity field. This leads to the development of several artifacts within the velocity volume. As seen in the depth sections presented in Appendix A1.1 to A1.25, isolated velocity highs produced along the eastern end of Line1, result from this interpolation. In addition, a "bulls-eye" shaped velocity high, shown at the beginning of Line 1 in Appendix A1.10 to A1.18 is due to the isolation of data points in this region (see Figure 2).

7. Conclusions:

Analysis of the ambient noise record recorded by the three arrays presented in Figure 2 successfully achieved the goal of refinement the basin structure and characterization of shear-wave velocities in the upper 1 km of the surface. The 2D shear-wave representations presented in Figures 9, 10, and 11 provide a more accurate depiction of the basin shape than previously available and highlight regions where more detailed future studies should occur to improve these results. The 2D models do not highlight the location of major structural faults. If present, faults traversed by these arrays do not significantly displace sediments with considerable velocity contrast beneath 50 m depth. While small scale near-surface faults may be present in the upper 50 m, which may manifest appreciable velocity contrasts, due to the large station spacing of 100 m and 200 m, these are not able to be characterized by this study. Array lengths with denser measurements are required to characterize the near-surface.

In effect, this project was very much a pilot study to test the ability of the ReMi technique to define the shear-wave velocity structure of the Reno-area basin. Prior to data collection, it was recognized that the length of the arrays would determine the depth of resolution of the data and that spacing was critical in defining the clarity of the data. However the comparison of the dispersion images shown in Figures 6, 7, and 8 clearly show that 100 m spacing more clearly delineates the Rayleigh wave energy. Future studies within the Reno-area basin will benefit from this knowledge, allowing acquisition of better clarity data. Use of lower frequency geophones may enhance imaging of low frequency Rayligh waves, but improvement will be minor compared to the effect of the ideal station spacing.

8. Further refinements:

One possible caveat of these shear-wave velocity models is the trade-off between velocity and depth. We propose to refine this 3D velocity model through use of cross-correlation and auto-correlation of the ambient noise records to image the geological structure beneath the arrays. Using seismic interferometry through cross-correlation and auto-correlation the P reflection time section from the ambient noise records is recovered. Stacking of these results over time windows will allow generation of a virtual shot gather. Processing of these virtual shot gathers will result in an image of the Earth's reflection response beneath each of the three arrays. Seismic interferometry has been tested through a pilot study with comparison of active source data across two seismic lines gathered in Nevada. Ambient noise data were recorded over three consecutive days at sensors co-located along the location of two active seismic reflection array lines. Comparison of processed noise cross-correlation data with the traditional active seismic reflection record sections show encouraging similarities (Tibuleac *et al.*, 2010). One downfall of that pilot study was the lack of surface ambient noise and poor azimuthal coverage of noise sources. The urban setting of the data analyzed under this proposal overcomes these data limitations, enhancing the potential of obtaining detailed seismic reflection images.

Noise sources from the urban setting of the data from this study will provide detailed waveform data to image subsurface structure. The abundant cultural noise from all azimuths, make this data ideal and affords us a unique opportunity to apply this new imaging method. Depths to prominent material interfaces with high impedance contrasts can be identified from these sections, including the basin bottom. These depths will place additional constraints on the forward modeling of the Rayleigh-wave dispersion data used to invert for the velocity-depth structure beneath each array. The resultant seismic interferometric reflection image will also more clearly highlight the existence and location of localized faulting in the area along with other geological features such as discontinuities.

Acknowledgements:

We thank Dr. John Louie and his team of students for their help with field deployment, and monitoring of the seismic instruments. Dr. Pat Cashman and Prof. Jim Trexler provided useful discussion and insight on the interpretation of the results.

References:

Abbott, R. E., and Louie J. N. (2000). Depth to bedrock using gravimetry in the Reno and Carson City, Nevada area basins, *Geophysics*, 65, 340-350.

Adams, K.D., and Sawyer, T.L., compilers (1999a). Fault number 1646, Unnamed fault zone in the Truckee River canyon, in *Quaternary fault and fold database of the United States: U.S. Geological Survey website*, http://earthquakes.usgs.gov/regional/qfaults, accessed 10/23/2012 05:48 PM.

Adams, K.D., and Sawyer, T.L., compilers (1999b), Fault number 1655, Unnamed fault zone east of Reno, in *Quaternary fault and fold database of the United States: U.S. Geological Survey website*, http://earthquakes.usgs.gov/regional/qfaults, accessed 10/25/2012 02:18 PM.

Bell, J. W, and H. F. Bonham (1987). Vista Quadrangle Geologic Map, Nevada Bureau of Mines and Geology, Map 4Hg, 1:24,000 scale.

Bell, J. W, and L. J. Garside (1987). Verdi Quadrangle Geologic Map, Nevada Bureau of Mines and Geology, Map 4Gg, 1:24,000 scale.

Bell, J. W., Watters, R. J., and Glancy, P. A. (1989) Engineering geology of the Reno-Lake Tahoe area, Nevada: in Hanshaw, P. M., Ed., *Environmental, engineering, and urban geology, in the United States*; 2, Engineering geology of the western United States urban centers, 41-50.

Bingler, E. (1975). *Guidebook to the Quaternary Geology along the Western Flank of the Truckee Meadows, Washoe County, Nevada*, Nevada Bureau of Mines and Geology, Report 22, 18 p.

Blakely,R. J., Hachens, R.C., Calzia, J. P., and V. E. Langenheim (1999) Cenozoic basins of the Death Valley extended terrane as reflected in regional-scale gravity anomalies, in Wright, L. A., and Troxel, B.W., Eds., *Cenozoic basins of the Death Valley region*, Geol. Soc. Am. Spec. Paper 333.

Bonham, H. F., and E. C. Bingler (1973). Reno Folio Geologic Map, Nevada Bureau of Mines and Geology, Environmental Series, Map 4Ag, 1:24,000 scale.

Bonham, H. F., and D. K. Rogers (1983). Mt Rose NE Quadrangle Geologic Map, Nevada Bureau of Mines and Geology, Map 4Bg, 1:24,000 scale.

Clark, M., J. Louie, A. Pancha, J. Scott, and K. Heath (2005). Geophysical investigation of a fault as a hydrologic barrier in Reno, Nevada: presented at the Seismol. Soc. of Amer. Ann. Mtg., Lake Tahoe, Nevada, April 26-29.

Dhar, M. Thompson, A. Kell-Hills, J.N. Louie, and K.D. Smith (2009), Station delays and their variance in the Reno-area basin from a dense deployment during the 2008 West Reno earthquake swarm, Eos Trans. AGU, 90(52), Fall Meet. Suppl., Abstract U53A-0062.

dePolo, C. M., J. G. Anderson, D. M. dePolo, and J. G. Price (1997). Earthquake occurrence in the Reno-Carson city urban Corridor, Seismological Research Letters, 68, p. 401-412.

Frary, R. N., J. N. Louie, W. J. Stephenson, J. K. Odum, L. Liberty, S. Pullammanappallil, N. Prina, P. Cashman, J. Trexler, and R. L. Kent (2001). 3D Controls on Basin Structure from a Network of High-Resolution Seismic Imaging Profiles in South Reno, Nevada, *Abstract, Seismological Research Letters*, 82(2), 298, presented at the *Seismological Society Annual Meeting*, 13-15 April, Memphis, Tennessee.

Frary, R. (2012). *Fault imaging with high-resolution seismic reflection for earthquake hazard and geothermal resource assessment in Reno, Nevada*. (University of Nevada, Reno).

ProQuest Dissertations and Theses, , 58. Retrieved from http://search.proquest.com/docview/1022626287?accountid=452

Heath, R. (2011). Time to consider the practicalities of passive seismic acquisition, *First Break*, 29 (7), 91-98.

Hess, R.H., and G Johnson (2000). County digital maps of Nevada, Nevada Bureau of Mines and Geology, Open-File Report 97-1, CD-ROM.

Hittelman, A.D., Dater,D., Buhmann, R., and S. Racey (1994). Gravity CD-ROM and user's manual, National Oceanic and Atmospheric Administration, National Geophysical Data Center.

Jachens, R. C., and B. C. Moring (1990). *Maps of thickness of Cenozoic deposits and isostatic residual gravity over basement in Nevada*, U.S. Geol. Surv. Open-File Report 90–404.

Louie, J. N., 2001, Faster, better: Shear-wave velocity to 100 meters depth from refraction microtremor arrays, *Bull. Seism. Soc. Amer.*, ***91***, 347-364.

Louie, J., I. M. Tibuleac and L. Preston (2010). *Basin Model Improvements and Verification for Reno Area, a 3-D Scenario Modeling*, final report on grant 08HQGR0046, http://earthquake.usgs.gov/research/external/reports/08HQGR0046.pdf.

Odum, J. K., W. J. Stephenson, R. N. Frary, G. C. Schmauder, and J. N. Louie (2001). Shallow 3.5 km Long, Shear-wave Velocity Profile in Reno, Nevada Derived from Ambient Noise Analysis of Uncorrelated P-wave Minivib Data, *Abstract, Seismological Research Letters*, 82(2), 299, presented at the *Seismological Society Annual Meeting*, 13-15 April, Memphis, Tennessee.

Pancha, A., J.G. Anderson, J.N. Louie, and A. Anooshehpoor, Data and simulation of ground motion for Reno, Nevada, 13th World Conference on Earthquake Engineering, Vancouver, B.C., Canada, Aug. 1-6, 2004, Paper No. 3452, 2004.

Pancha, A., J. Anderson, and J. Louie (2007a). Characterization of near-surface geology at strong-motion stations in the vicinity of Reno, Nevada, *Bull. Seismol. Soc. Amer.*, **97**, 2096-2117, doi: 10.1785/0120060266.

Pancha, A. (2007b). Seismic Hazards in the Basin and Range province, U.S.A., *Ph.D Dissertation, University of Nevada, Reno*, 382 p.

Pancha, A., J. G. Anderson, J. N. Louie, S. Pullammanappallil, (2008). Measurement of shallow shear wave velocities at a rock site using the ReMi technique, Soil *Dynamics and Earthquake Engineering*, 28, 522-535.

Park, C. B., R. D. Miller, and J. Xia (1999). Multichannel analysis of surface waves, *Geophysics* 64, 800–808.

Preston, L., and D. von Seggern, Joint Seismic Tomography/Location Inversion in the Reno/Carson City Area, *Final Report to the National Earthquake Hazard Reduction Program*, U. S. Geological Survey Award Number 07HQGR0022, 2008.

Sawyer, T.L., compiler, (1999). Fault number 1647, Mount Rose fault zone, in *Quaternary fault and fold database of the United States: U.S. Geological Survey website*, http://earthquakes.usgs.gov/regional/qfaults, accessed 10/23/2012 05:42 PM.

Scott, J. B., M. Clark, T. Rennie, A. Pancha, H. Park, and J. N. Louie (2004). A shallow shear-wave velocity transect across the Reno, Nevada area basin, *Bull. Seismol. Soc. Amer*., 94, 2222-2228.

Stephenson, W. J., R. N. Frary, J. N. Louie, and J. K. Odum (2012). Extensional growth faulting beneath Reno, Nevada, imaged by urban seismic profiling, [in review].

Tibuleac, I. M., D von Seggern, J Louie and J Anderson (2009). High resolution seismic velocity structure in the Reno Basin from ambient noise recorded by a variety of instruments, *Geothermal Resources Council 3rd Annual Meeting*, Oct 4-7, 2009, Reno NV, U.S.A.

Tibuleac, I.M.; Pullammanappallil, S.; von Seggern, D. H.; Pancha, A.; Louie, J. N., (2010). Retrieval of Earth's reflection response from ambient seismic noise - a Nevada experiment, *American Geophysical Union, Fall Meeting 2010, abstract #S33A-2071*

Tibuleac, I. M., D. H. von Seggern, John G. Anderson and J.N. Louie (2011). Computing Green's Functions from Ambient Noise Recorded by Narrow-Band Seismometers, Accelerometers, and Analog Seismometers, doi: 10.1785/gssrl.82.5.661 *Seismological Research Letters*, September/October 2011 v. 82 no. 5 p. 661-675.

Trexler, J. H., P. H. Cashman, C. D. Henry, T. Muntean, K. Schwartz, A. TenBrink, J. E. Faulds, M. Perkins, and T. Kelly (2000). Neogen basins in western Nevada document the tectonic history of the Sierra Nevada-Basin and Range transition zone for the last 12 Ma, in *Great Basin and Sierra Nevada*, D. R. Lageson, S. G. Peters and M. M. Lahren (Editors), Boulder, Colorado, Geological Society of America Field Guide 2, 97–116.

Widmer, M. (2005). Gravity-based geological modeling of the Central Truckee Meadows, prepared for The Central Truckee Meadows Remediation District, Washoe County Department of Water Resources.

Widmer, M. C., Cashman, P. H., Benedict, F. C., and J. H. Trexler (2007). Neogene through Quaternary Stratigraphy and Structure in a Portion of the Truckee Meadows Basin: A Record of Recent Tectonic History, presented at the *Geological Society of America Cordilleran Section*, 103rd Annual Meeting.

Table 1(a): Instrument groupings used to obtain 1D shear-wave velocity soundings along Line 1 (see Figure 2 for location). Average velocities to 10-, 30-, 50-, and 100-meter depths, denoted Vs10[§], Vs30[§], Vs50, and Vs100, respectively are listed along with the depths where the shear velocity first exceeds0.5 km/s, 1.0 km/s, 1.5 km/s, and 2.0 km/s (Z0.5, Z1.0, Z1.5, and Z2.0 respectively).

Station Spread	Midpoint		Velocity, m/s				Depth, m			
	Latitude	Longitude	Vs10[§]	Vs30[§]	Vs50	Vs100	Z0.5	Z1.0	Z1.5	Z2.0
101 to 115	39.5008	-119.8706	253.24	290.37	352.36	484.87	22.50	163.75	327.50	327.50
102 to 116	39.5014	-119.8673	253.24	271.78	335.64	456.18	26.00	140.00	467.50	467.50
103 to 117	39.5016	-119.8648	235.57	258.99	307.98	439.88	50.00	140.00	467.50	467.50
104 to 118	39.5013	-119.8608	288.59	299.15	317.76	437.53	50.00	161.25	620.00	620.00
105 to 119	39.5008	-119.8589	217.90	235.68	269.05	406.17	50.00	98.75	662.50	662.50
106 to 120	39.5011	-119.8568	253.24	290.37	352.36	492.18	22.50	178.75	327.50	327.50
107 to 121	39.5019	-119.8547	253.24	350.28	427.41	602.00	13.75	95.50	210.00	210.00
108 to 122	39.5024	-119.8526	253.24	350.28	427.41	602.00	13.75	95.50	210.00	210.00
110 to 124	39.5040	-119.8484	253.24	369.91	447.01	598.01	11.50	130.00	210.00	210.00
111 to 125	39.5047	-119.8462	253.24	374.57	451.08	602.82	11.00	95.50	195.00	195.00
112 to 126	39.5049	-119.8439	429.53	429.53	429.53	533.03	50.00	212.00	265.00	265.00
113 to 127	39.5049	-119.8417	253.24	379.81	434.58	536.90	10.75	171.25	266.25	266.25
114 to 128	39.5051	-119.8392	253.24	379.81	434.58	536.90	10.75	171.25	266.25	266.25
116 to 130	39.5049	-119.8348	253.24	379.81	434.58	536.90	10.75	171.25	266.25	266.25

[§] Due to the large station spacing, velocities above 50 m depth are not well resolved.

Table 1(b): Instrument groupings used to obtain 1D shear-wave velocity soundings along Line 2 (see Figure 2 for location). Average velocities to 10-, 30-, 50-, and 100-meter depths, denoted Vs10[§], Vs30[§], Vs50, and Vs100, respectively are listed along with the depths where the shear velocity first exceeds0.5 km/s, 1.0 km/s, 1.5 km/s, and 2.0 km/s (Z0.5, Z1.0, Z1.5, and Z2.0 respectively).

Station Spread	Midpoint		Velocity, m/s				Depth, m			
	Latitude	Longitude	Vs10[§]	Vs30[§]	Vs50	Vs100	Z0.5	Z1.0	Z1.5	Z2.0
201 to 213	39.5056	-119.8636	382.21	382.21	382.21	430.96	185.00	918.24	918.24	918.24
204 to 218	39.5024	-119.8648	382.21	382.21	382.21	439.99	50.00	804.81	804.81	804.81
205 to 219	39.5015	-119.8648	400.78	400.78	400.78	428.82	167.50	535.00	620.00	620.00
206 to 220	39.5005	-119.8649	400.78	400.78	400.78	428.82	167.50	465.00	602.50	602.50
207 to 221	39.5005	-119.8618	400.78	400.78	400.78	428.82	152.50	417.50	560.00	560.00
208 to 222	39.4996	-119.8622	400.78	400.78	400.78	428.38	140.00	442.50	560.00	560.00
209 to 223	39.4988	-119.8622	382.21	382.21	382.21	430.96	157.50	530.00	530.00	530.00
210 to 224	39.4978	-119.8625	403.47	403.47	403.47	444.15	137.50	535.00	535.00	535.00
211 to 225	39.4971	-119.8632	382.21	382.21	382.21	430.96	157.50	430.00	430.00	430.00
212 to 226	39.4965	-119.8639	382.21	382.21	428.63	499.38	35.00	407.50	407.50	407.50
213 to 227	39.4960	-119.8648	382.21	382.21	428.63	499.38	35.00	407.50	407.50	407.50
214 to 228	39.4952	-119.8653	421.14	421.14	421.14	477.67	60.00	397.50	397.50	397.50
215 to 229	39.4943	-119.8658	415.44	415.44	415.44	465.14	50.00	374.25	374.25	374.25
216 to 230	39.4934	-119.8665	415.44	415.44	415.44	454.39	97.50	372.50	372.50	372.50

[§] Due to the large station spacing, velocities above 50 m depth are not well resolved.

Table 1(c): Instrument groupings used to obtain 1D shear-wave velocity soundings along Line 3 (see Figure 2 for location). Average velocities to 10-, 30-, 50-, and 100-meter depths, denoted Vs10[§], Vs30[§], Vs50, and Vs100, respectively are listed along with the depths where the shear velocity first exceeds0.5 km/s, 1.0 km/s, 1.5 km/s, and 2.0 km/s (Z0.5, Z1.0, Z1.5, and Z2.0 respectively).

Station Spread	Midpoint		Velocity, m/s				Depth, m			
	Latitude	Longitude	Vs10[§]	Vs30[§]	Vs50	Vs100	Z0.5	Z1.0	Z1.5	Z2.0
301 to 315	39.5096	-119.8844	394.63	394.63	394.63	446.89	50.00	407.50	580.00	580.00
303 to 317	39.5100	-119.8796	403.47	403.47	403.47	452.50	50.00	412.50	587.50	587.50
306 to 320	39.5109	-119.8729	394.63	394.63	394.63	446.89	50.00	377.50	670.00	670.00
308 to 322	39.5113	-119.8680	394.63	394.63	394.63	446.89	50.00	377.50	690.00	690.00
311 to 325	39.5121	-119.8614	394.63	394.63	394.63	446.89	50.00	360.00	687.50	687.50
313 to 327	39.5112	-119.8566	394.63	394.63	394.63	446.89	50.00	327.50	732.50	732.50
314 to 328	39.5108	-119.8544	394.63	394.63	394.63	446.89	50.00	387.50	675.00	675.00
315 to 329	39.5110	-119.8522	403.47	403.47	403.47	457.86	50.00	250.00	665.00	665.00
316 to 330	39.5117	-119.8498	403.47	403.47	403.47	452.50	50.00	312.50	712.50	712.50

[§] Due to the large station spacing, velocities above 50 m depth are not well resolved.

(a)

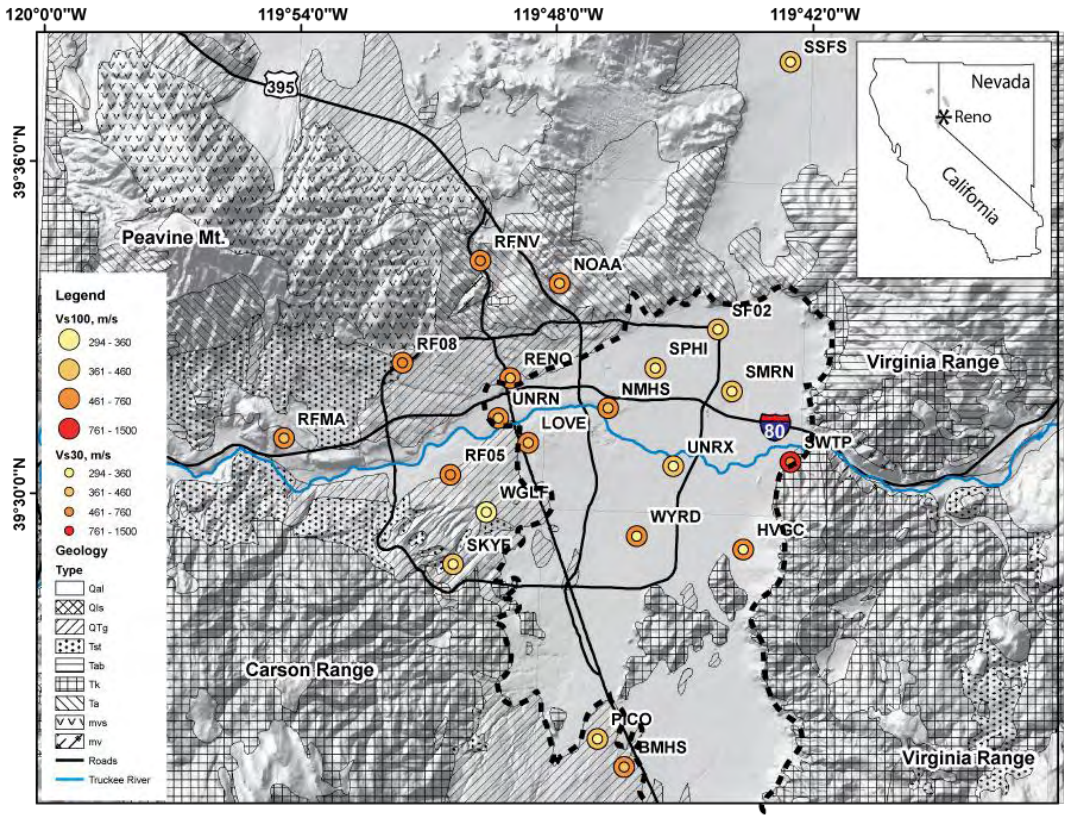

Figure 1(a): Topographic map of the Reno-area basin showing the location of the Advanced National Seismic System (ANSS) stations. Average shear wave velocity measurements to 30 m and 100 m (Vs30 and Vs100) at each station are also shown (Pancha *et al*. 2007a). The Truckee River is shown as a blue line. Geological units from the Nevada Bureau of Mines and Geology (NBMG) 1:250,000 digital geologic map (Hess and Johnson, 2000) are shown. These geological units are as follows: Qal, stream deposits; Qls, landslide deposits; Qtg, pre-Lake Lahontan deposits; Tst, Pliocene sedimentary rocks; Tab, basalt, basaltic, and andesite; Tk, Kate Peak formation, flows, or flow breccia; Ta, Alta Formation; mvs, Peavine Sequence, undifferentiated metavolcanics/metasediments; mv, Peavine Sequence, metavolcanic rocks. The extent of the Central Truckee Meadows is delimited by the extent of the Qal deposits enclosed by the dashed line. Inset shows the geographic location of Reno, Nevada, U.S.A.

(b)

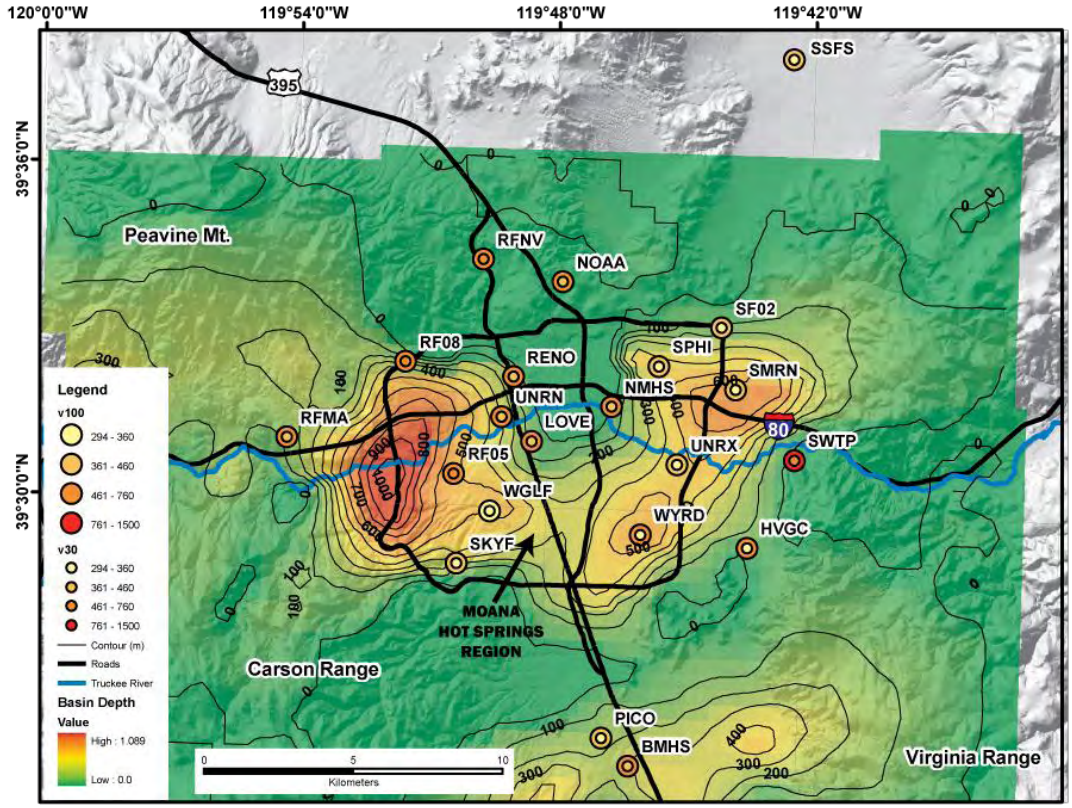

Figure 1(b): Basin depth model from Abbott and Louie (2000), based on gravity observations. Contours are 100 m. The formal name for the area is the Central Truckee Meadows, referring to the geomorphic flat region of Quaternary deposits. We refer to it as the Reno area basin after the largest city in the Reno–Sparks urban area, following Abbott and Louie (2000), incorporating both the geophysical and geomorphic expression of the basin.

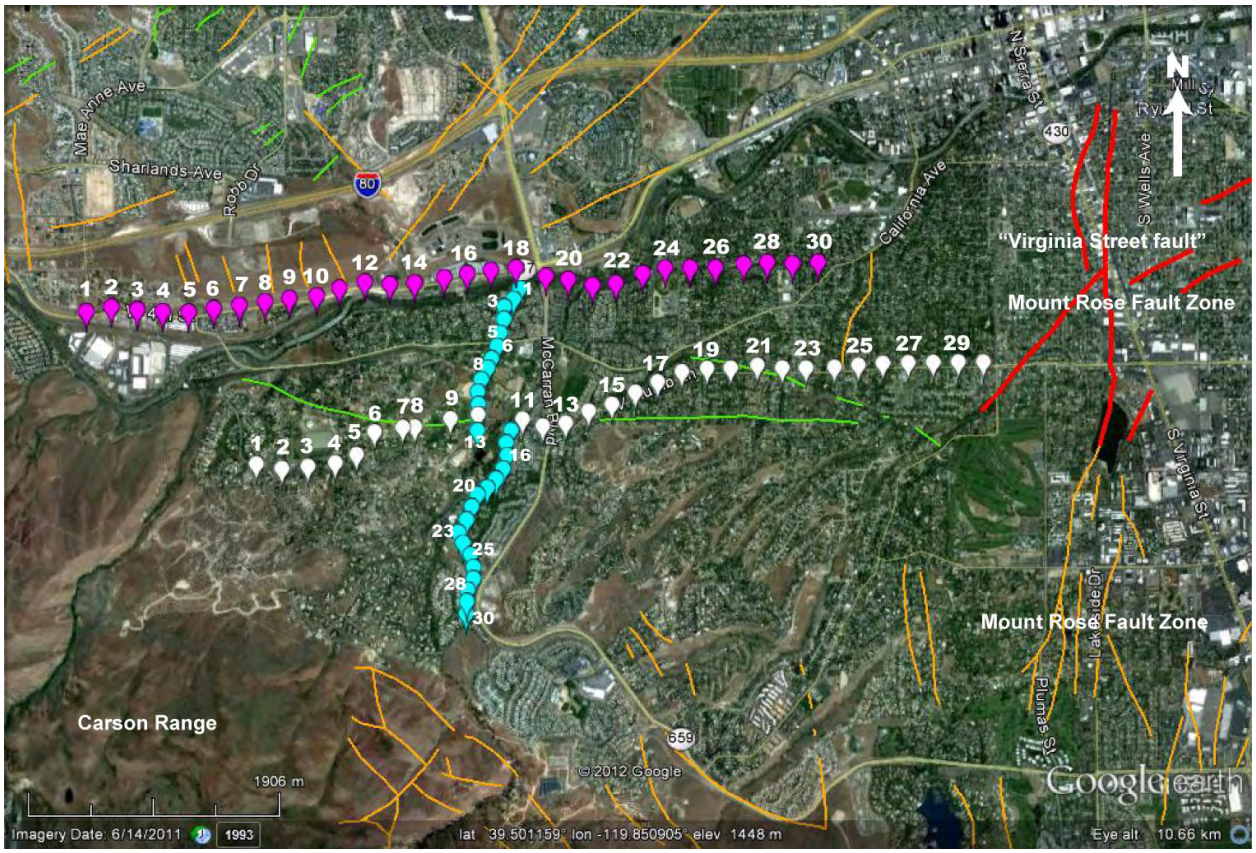

Figure 2: Locations of the long refraction microtermor (ReMi) arrays across the deepest portion of the basin obtained under award G12AP20026. Each array consisted of 30 wireless instruments, Line 1 (white) and Line 3 (pink) both have 200 m instrument spacing for a total array length of 5.8 km, while Line 2 (blue) is 2.9 km long with 100 m spacing. Also shown are the locations of the ANSS stations (yellow) and faults from the United States Geological Survey Quaternary fault and fold database (http://earthquakes.usgs.gov/regional/qfaults).

Figure 3: Pictures showing the Sigma™ cableless acquisition system by iSeis (Heath,2011). Each is powered by a 12-V battery and is connected to a single vertical P-wave geophone for this study.

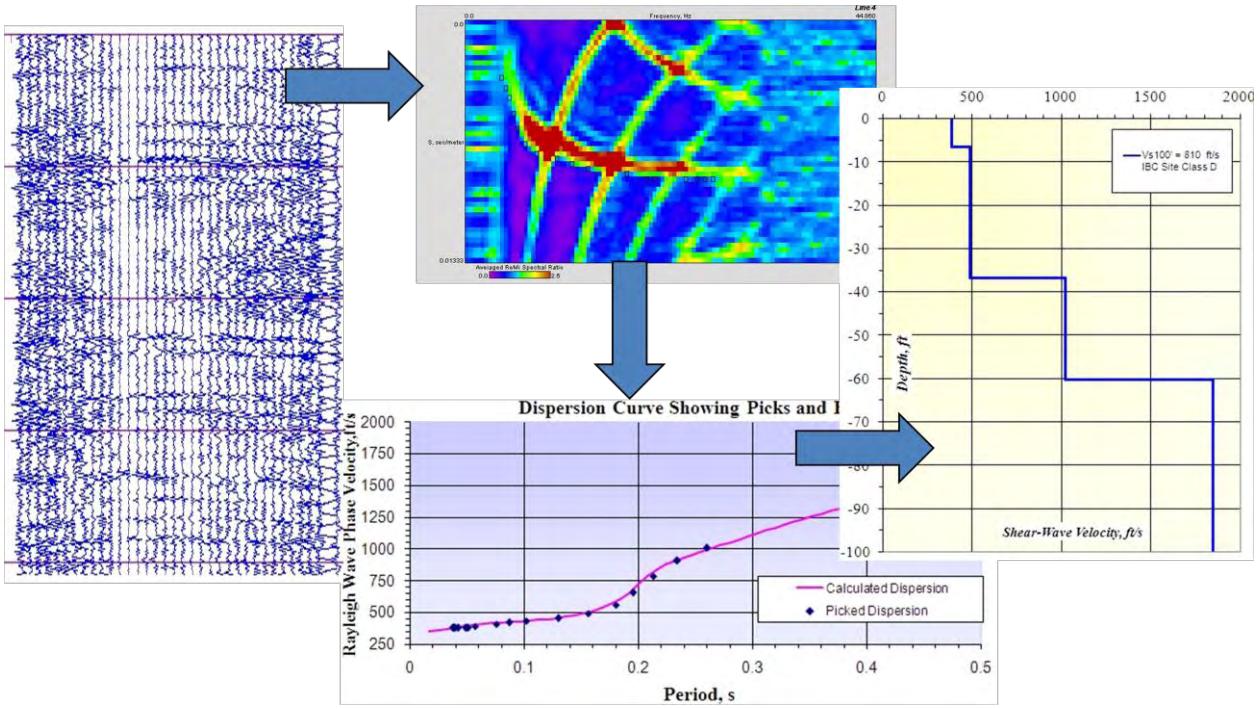

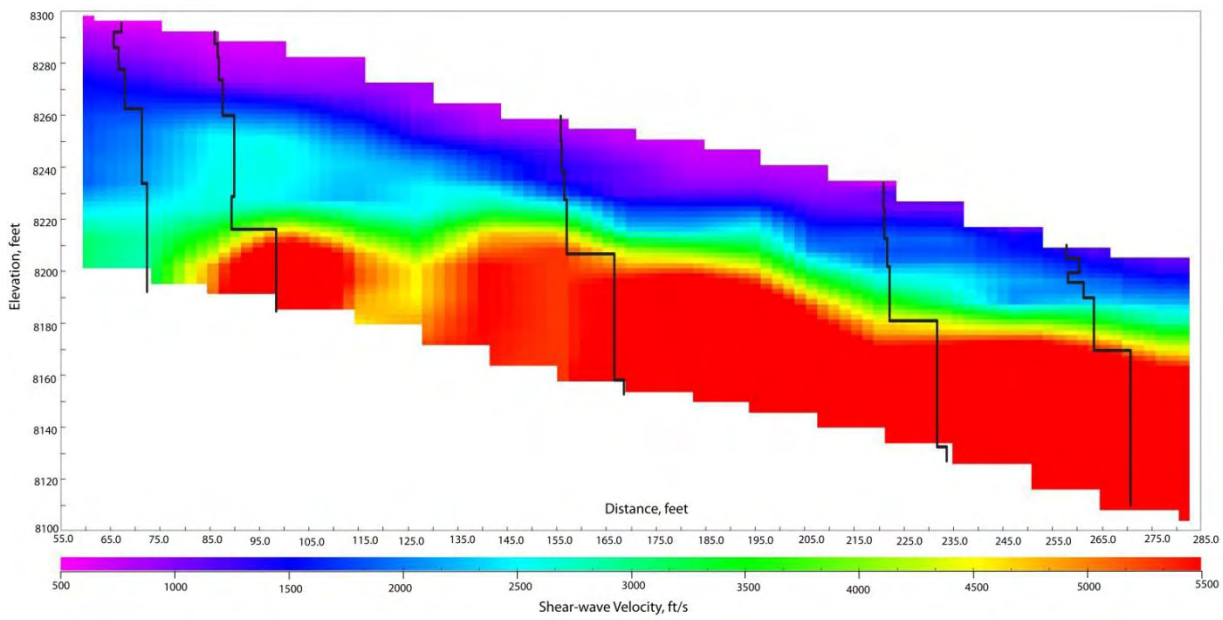

Figure 4. (top) Schematic of the ReMi™ process. Recorded microtremor data are first transformed into the frequency-slowness domain (Louie, 2001). The dispersion curve is then picked and modeled to obtain a 1D shear-wave velocity profile.
(bottom) Example of 2D Vs velocity modeled determined using 2D refraction microtremor analysis. The solid lines are the 1D profiles which are then interpolated to derive the 2D velocity structure. This image was produced using Optim's SeisOpt® ReMi™ software. The same technique will be employed to produce similar images along the locations proposed in Figure 3.

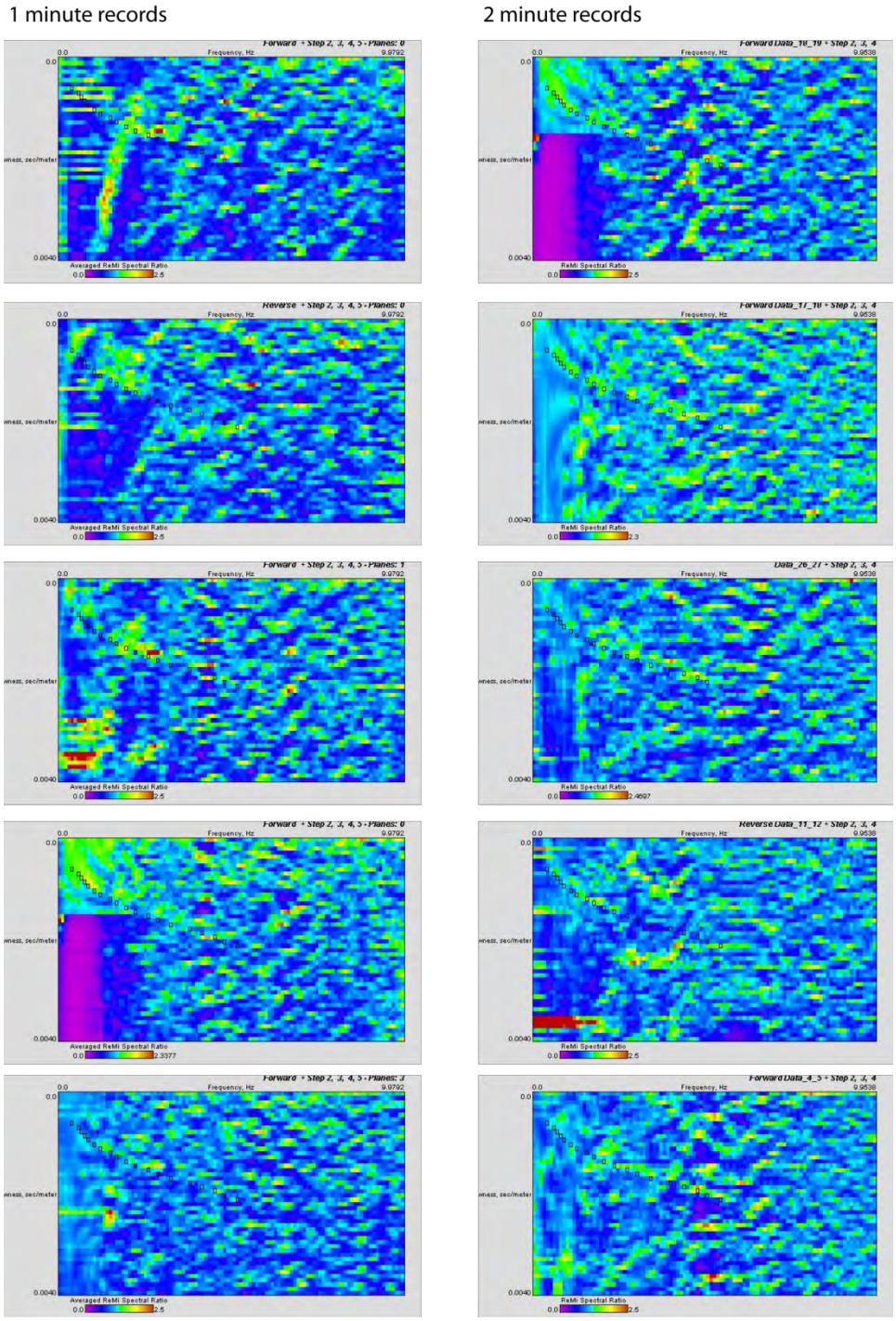

Figure 5: Comparison of dispersion curves calculated using all 30 instruments along Array#3 using 1 minute records (left) and 2 minute records (right). Each panel illustrated the slowness-frequency spectrum for a single one or two minute record. The black squares indicate the preferred lower envelope of the dispersion curve for all frequencies.

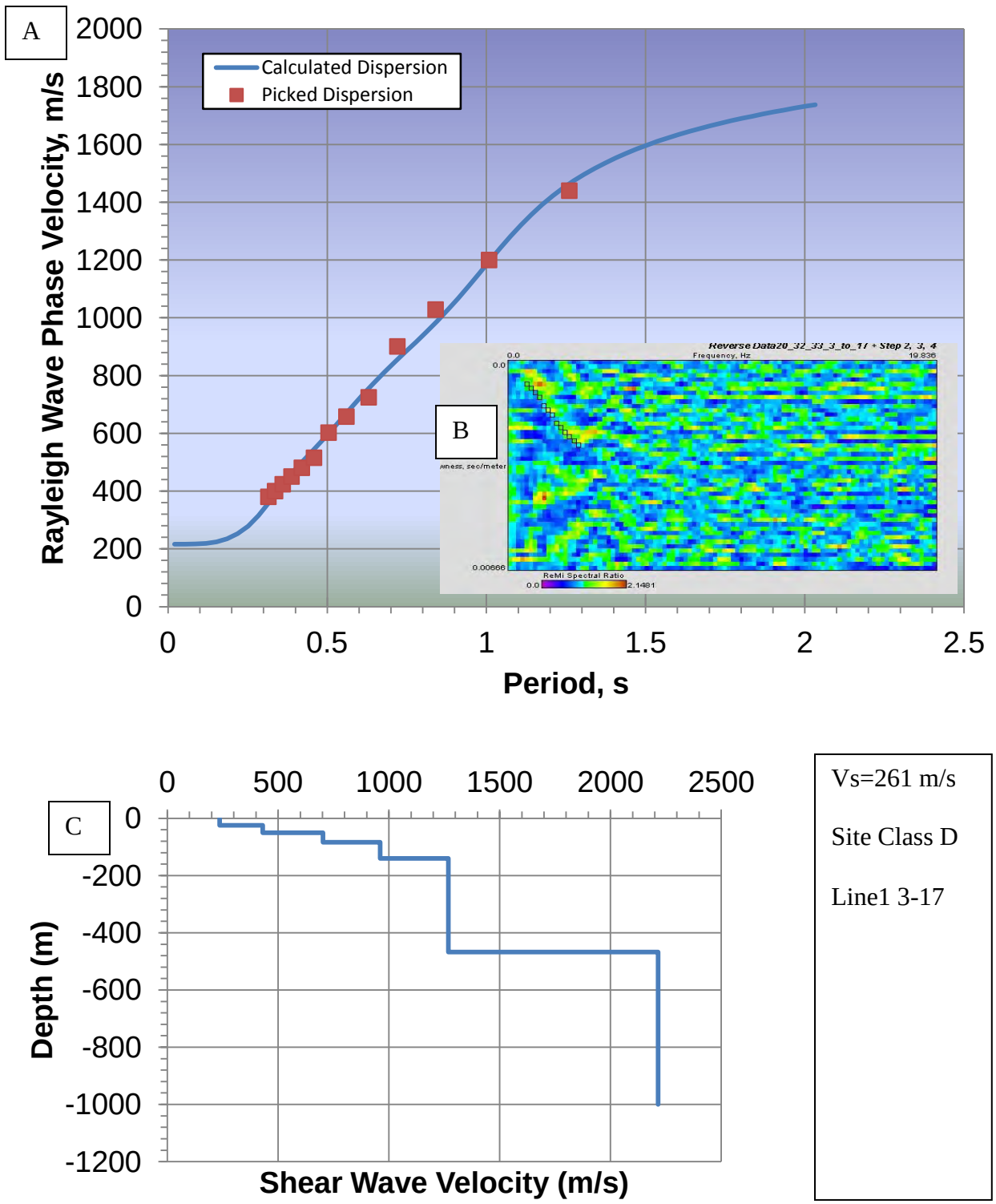

Figure 6: Example of ReMi analysis for a sample record along Line 1. Recorded microtremor data are first transformed into the frequency-slowness domain (Louie, 2001) **(A)**. The dispersion curve is then picked **(B)** and modeled to obtain a 1D shear-wave velocity profile **(C)**.

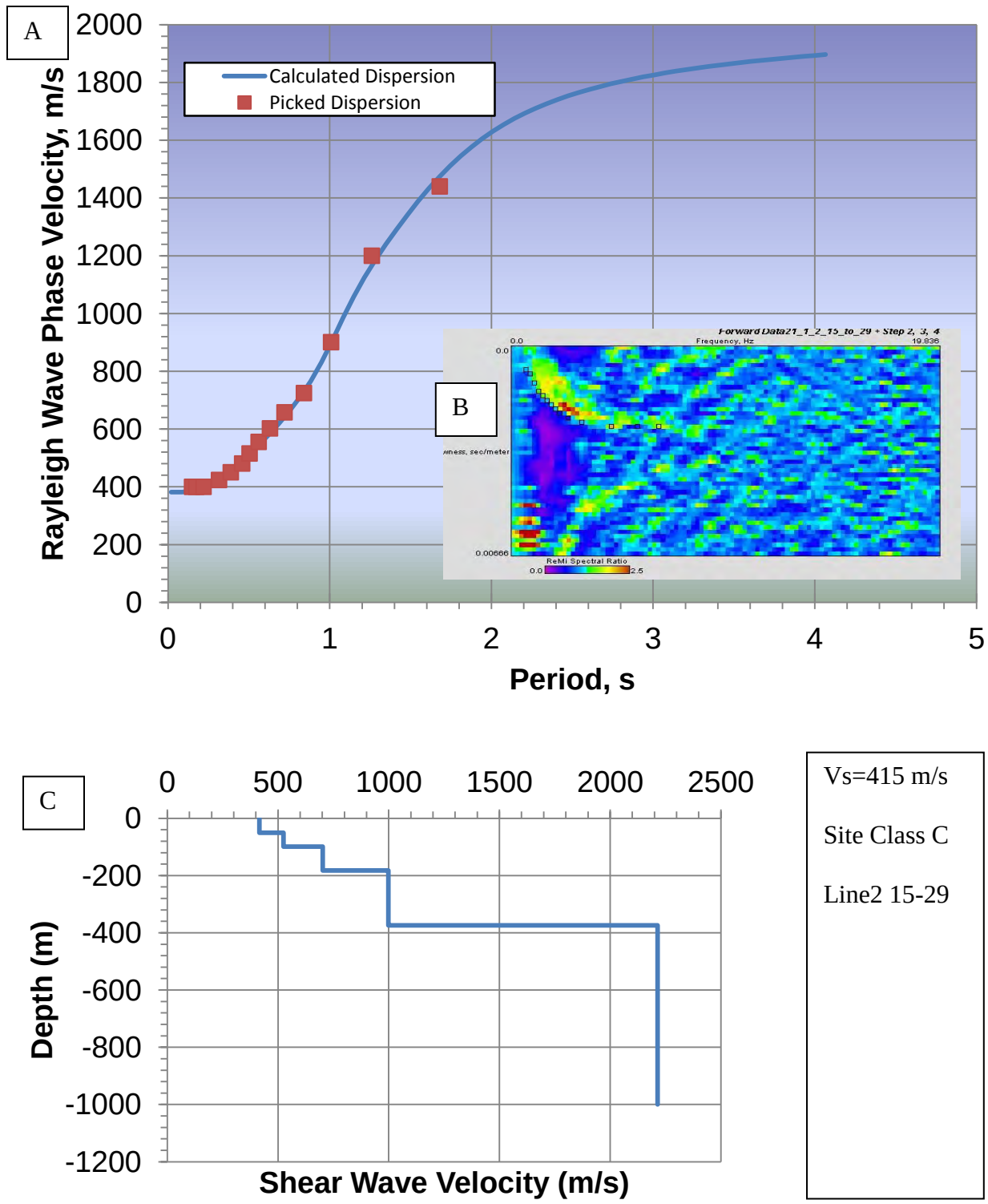

Figure 7: Example of ReMi analysis for a sample record along Line 2. Recorded microtremor data are first transformed into the frequency-slowness domain (Louie, 2001) **(A)**. The dispersion curve is then picked **(B)** and modeled to obtain a 1D shear-wave velocity profile **(C)**.

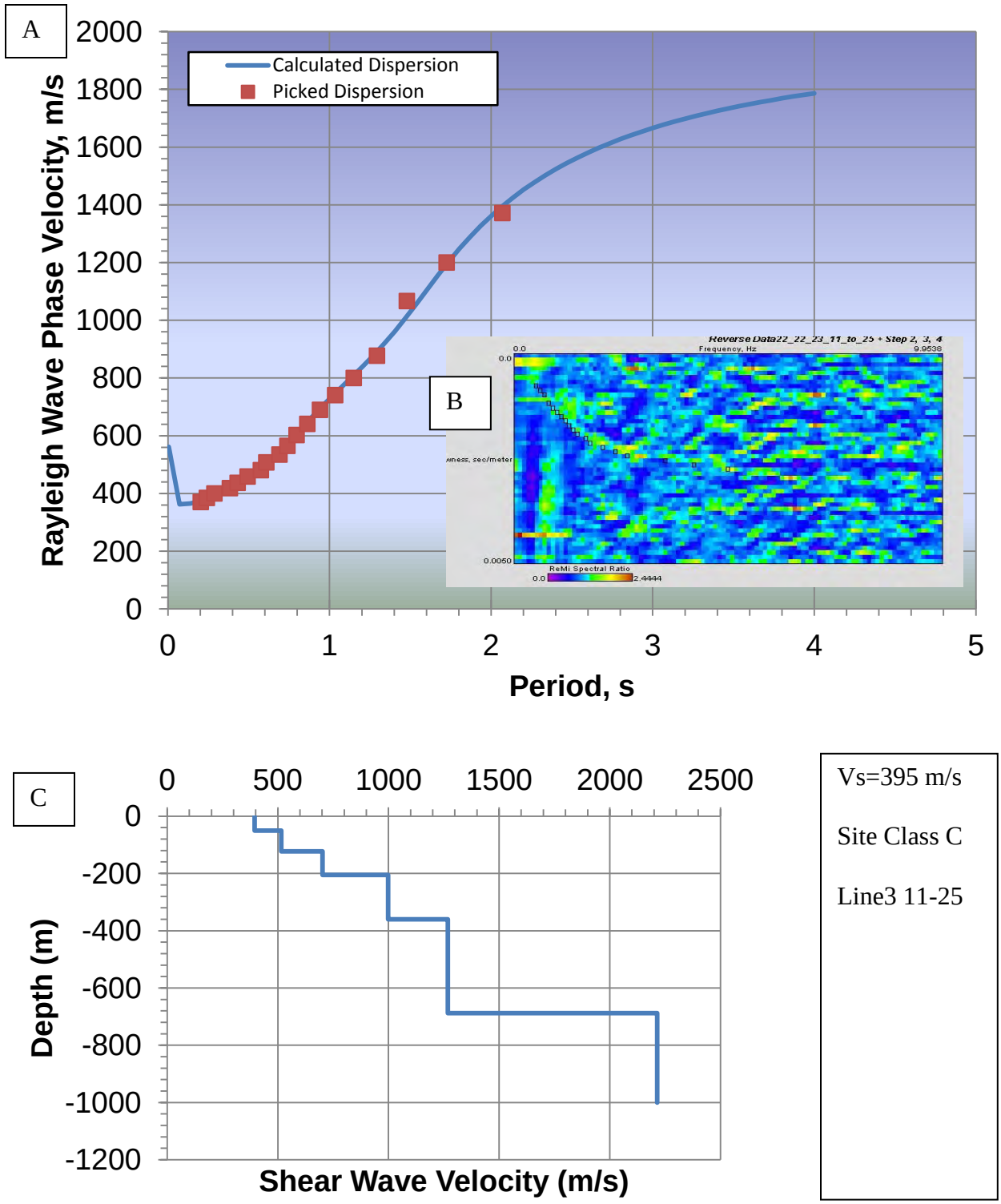

Figure 8: Example of ReMi analysis for a sample record along Line 3. Recorded microtremor data are first transformed into the frequency-slowness domain (Louie, 2001) **(A)**. The dispersion curve is then picked **(B)** and modeled to obtain a 1D shear-wave velocity profile **(C)**.

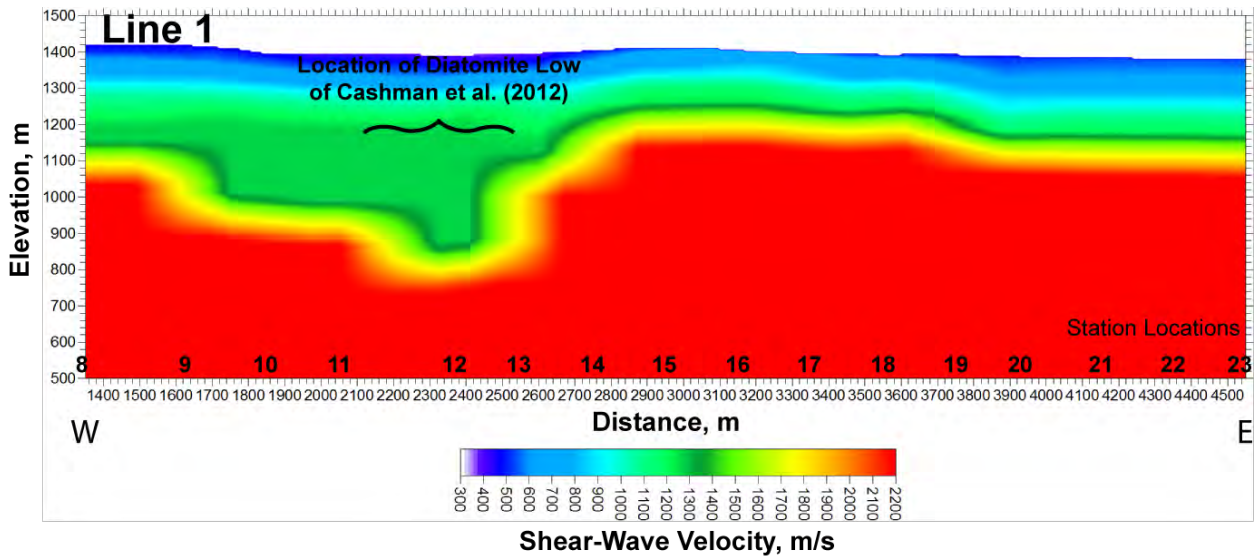

Figure 9: 2D Vs velocity modeled determined using 2D refraction microtremor analysis for Line 1. The image is compiled through interpolation of 1D shear-velocity profiles as function of depth determined from a moving array of 15 instruments along each line length. Distances along the array (assuming geophone 1 is located at 0 m) are show along the bottom. For referecnce Station numbers are shown in bold. The vertical axis shows elevation with top of the model at 1500 m.

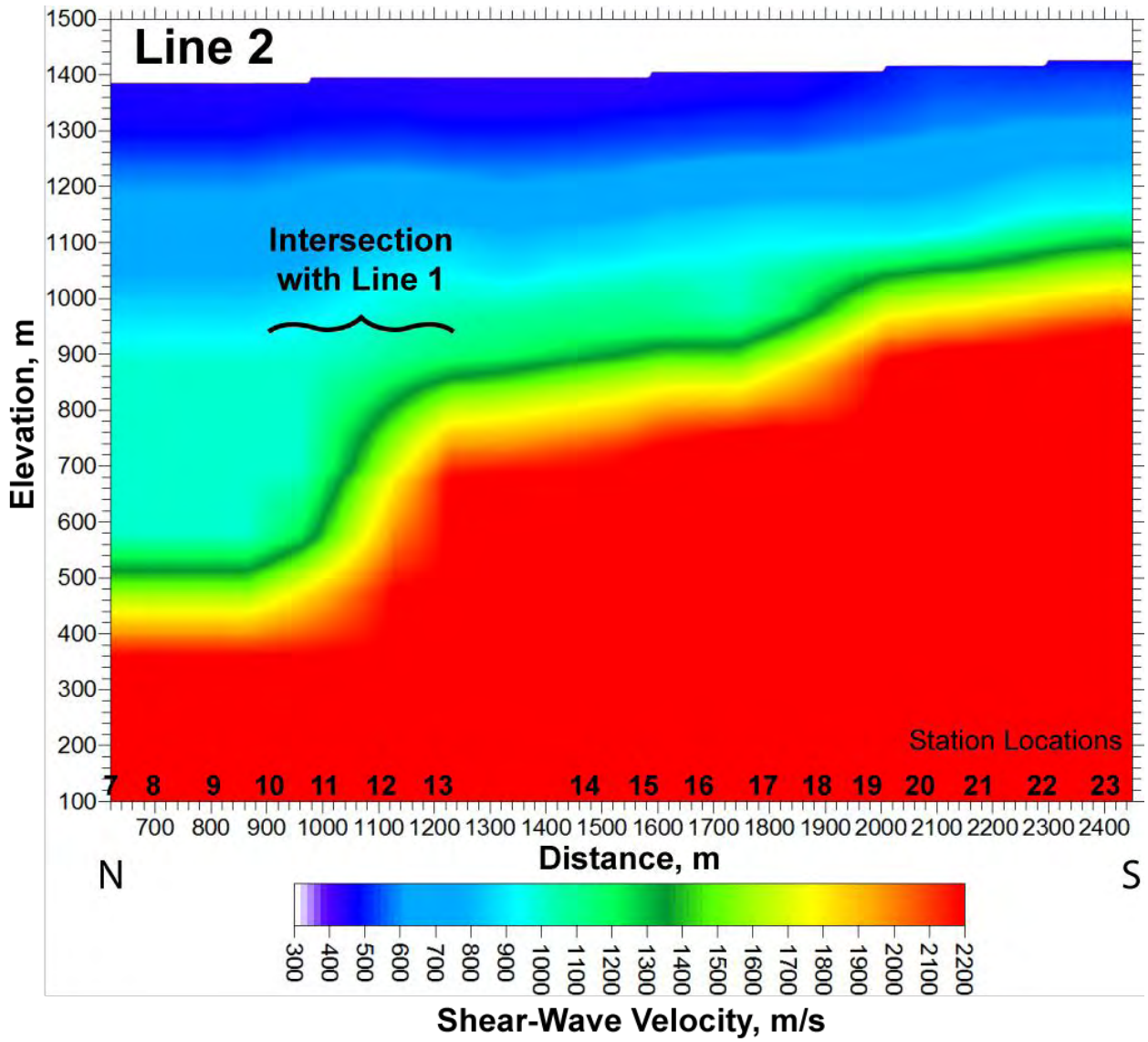

Figure 10: 2D Vs velocity modeled determined using 2D refraction microtremor analysis for Line 2. The image is compiled through interpolation of 1D shear-velocity profiles as function of depth determined from a moving array of 15 instruments along each line length. . Distances along the array (assuming geophone 1 is located at 0m) are show along the bottom. For referecnce Station numbers are shown in bold. The vertical axis shows elevation with top of the model at 1500 m.

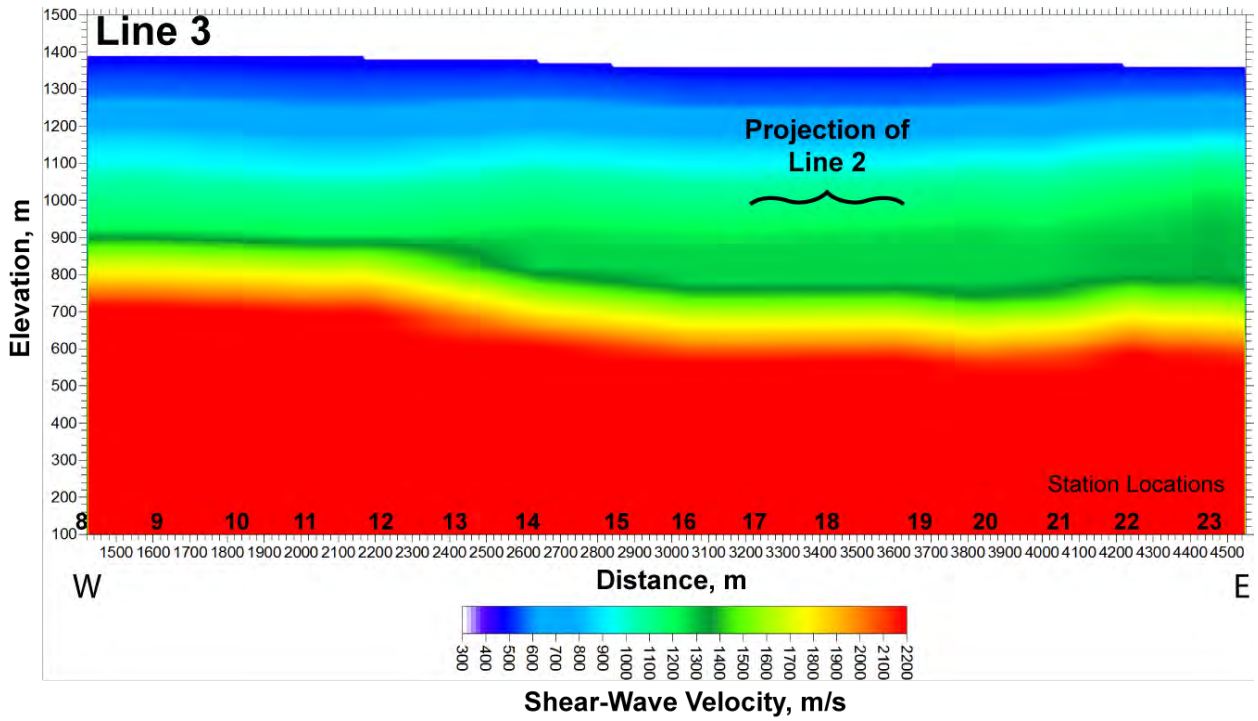

Figure 11: 2D Vs velocity modeled determined using 2D refraction microtremor analysis for Line 3. The image is compiled through interpolation of 1D shear-velocity profiles as function of depth determined from a moving array of 15 instruments along each line length. . Distances along the array (assuming geophone 1 is located at 0m) are show along the bottom. For referecnce Station numbers are shown in bold. The vertical axis shows elevation with top of the model at 1500 m.

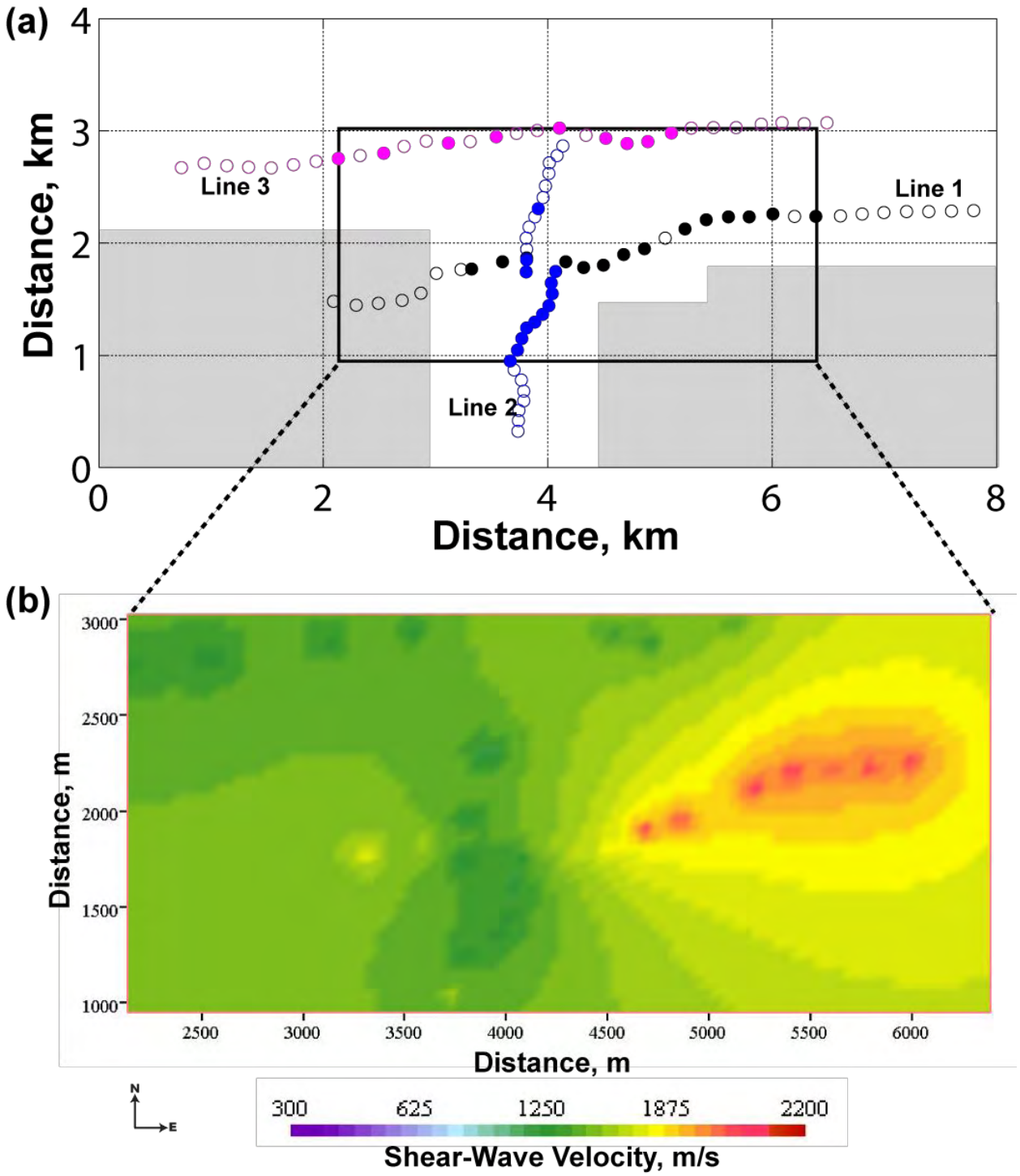

Figure 12: (a) Schematic showing the location of the stations (circles) along each line. Midpoints of the 15 station sub-arrays analyzed to produce the 2D representations in Figures 6, 7 and 8 are displayed as solid circles. The inset box shows the extent of the 3D volume. (b) Slice through 3D velocity representation at 250 m depth showing effects of the 3D interpolation routine.

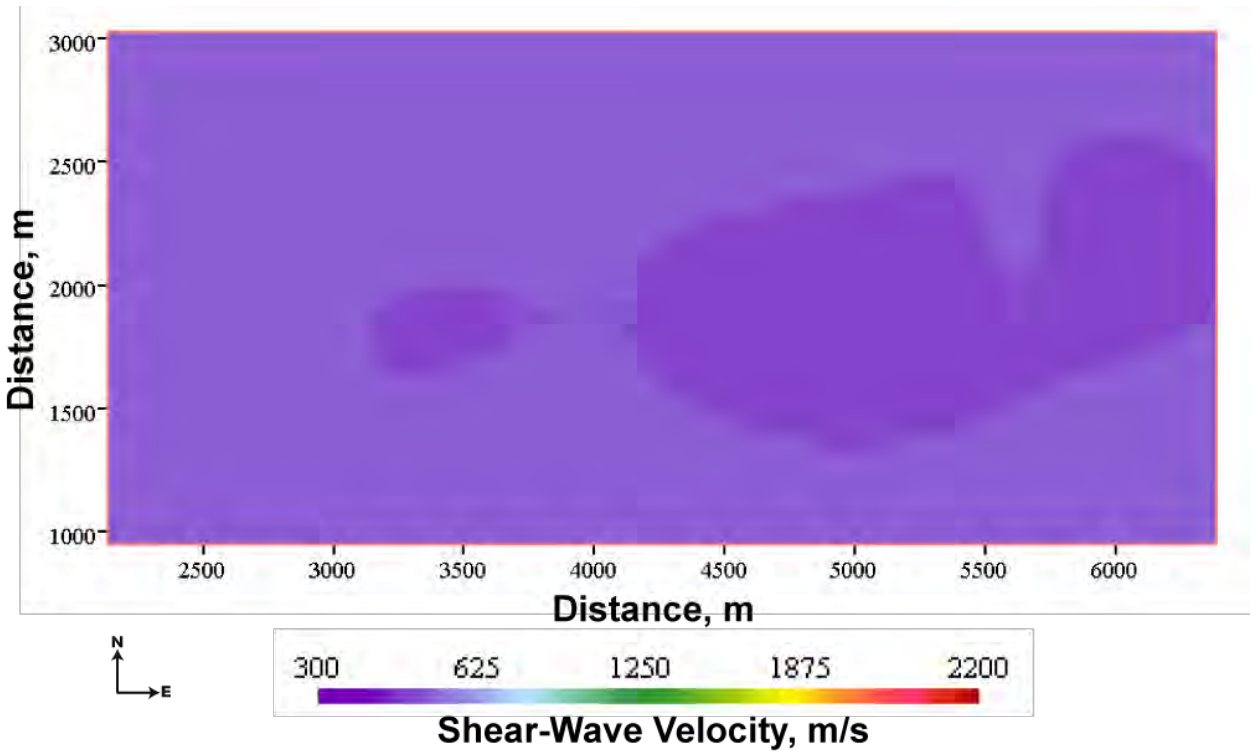

Appendix 1.1: Slice through 3D shear-wave velocity representation at 0 m depth.

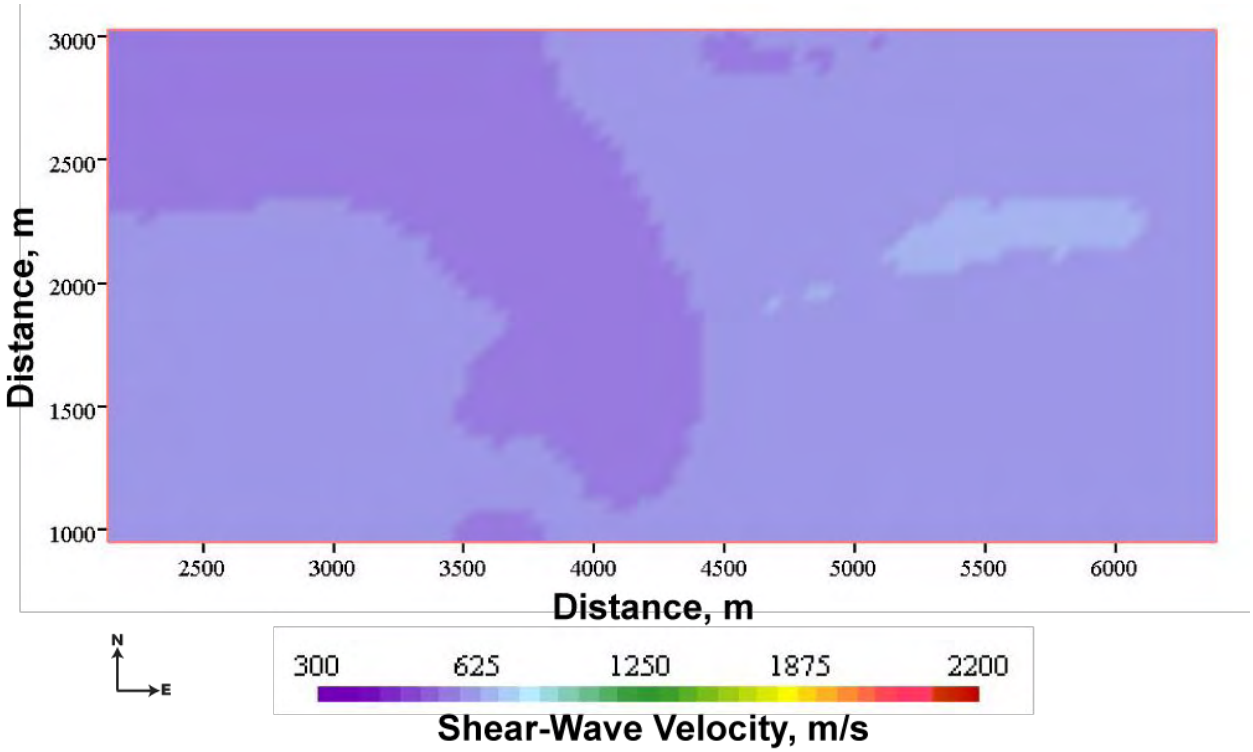

Appendix 1.2: Slice through 3D shear-wave velocity representation at 25 m depth.

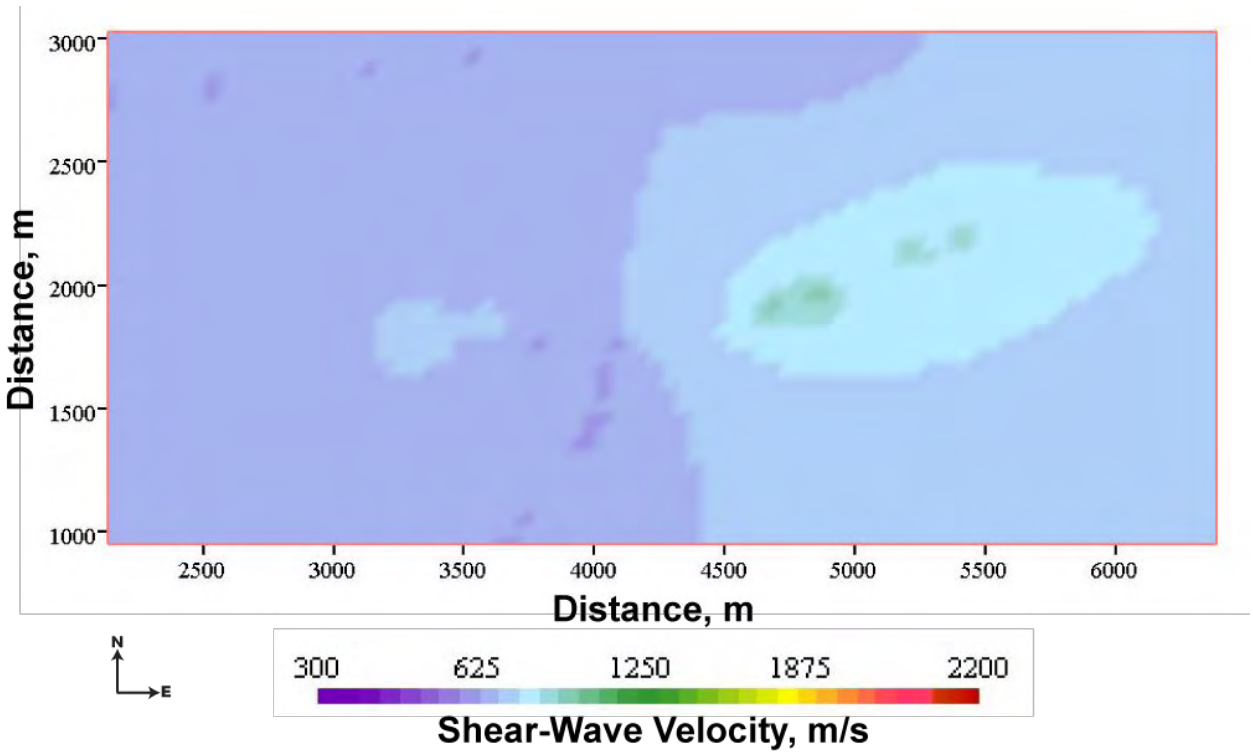

Appendix 1.3: Slice through 3D shear-wave velocity representation at 50 m depth.

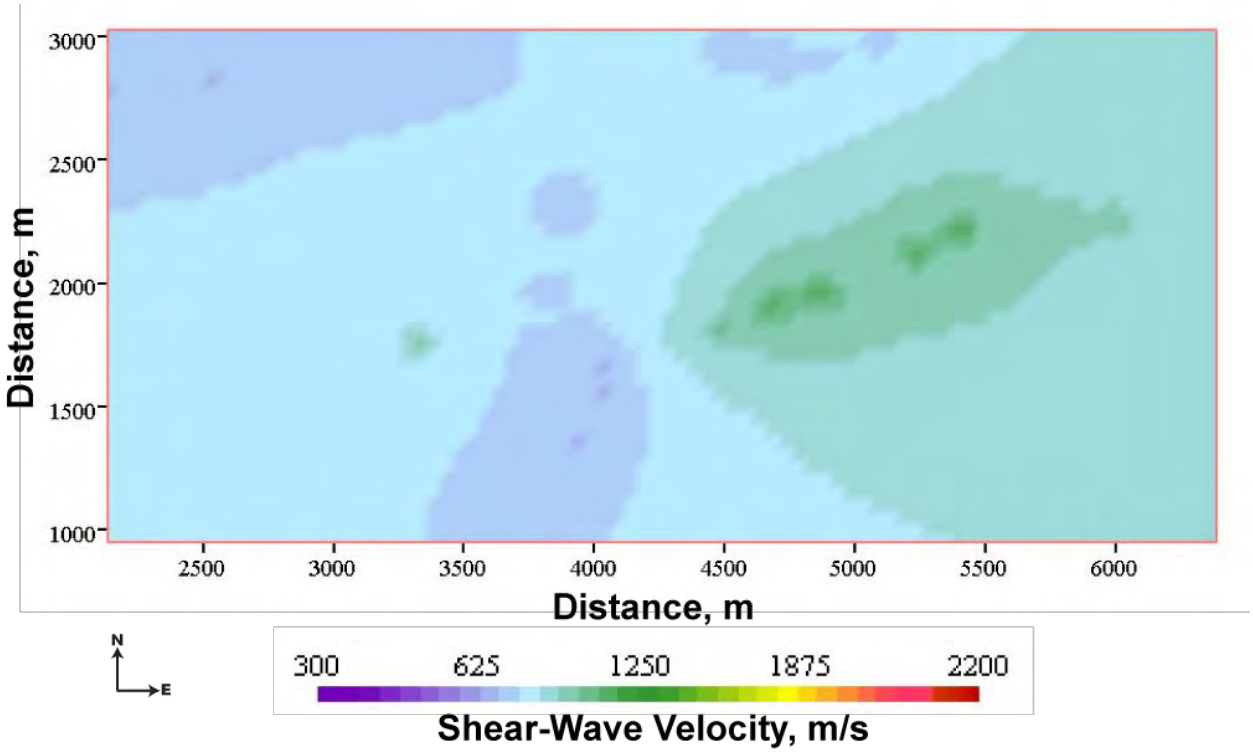

Appendix 1.4: Slice through 3D shear-wave velocity representation at 75 m depth.

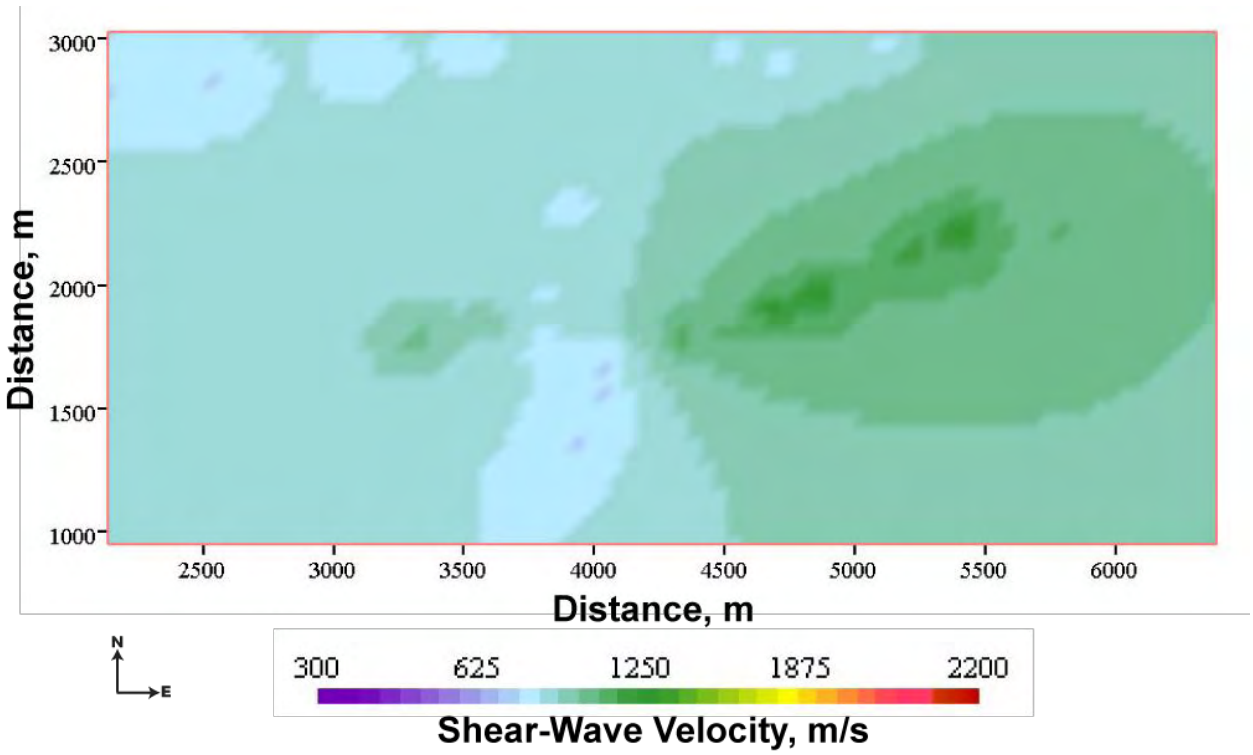

Appendix 1.5: Slice through 3D shear-wave velocity representation at 100 m depth.

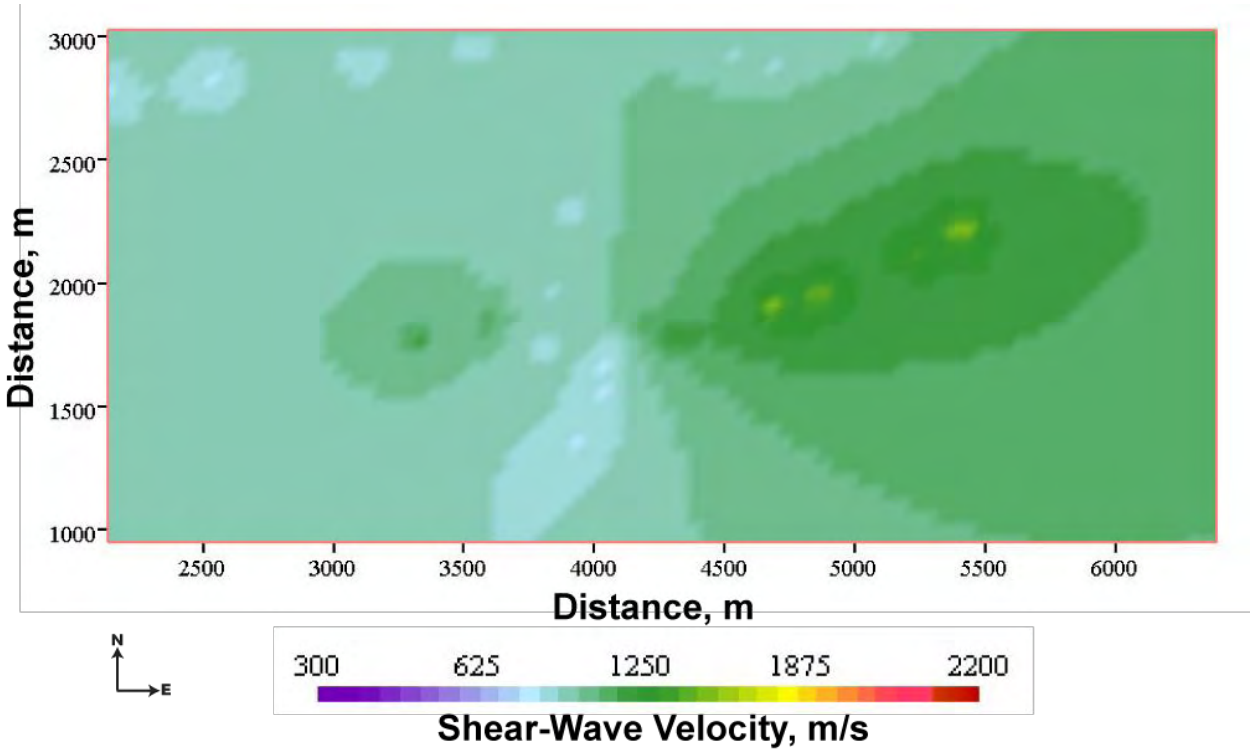

Appendix 1.6: Slice through 3D shear-wave velocity representation at 125 m depth.

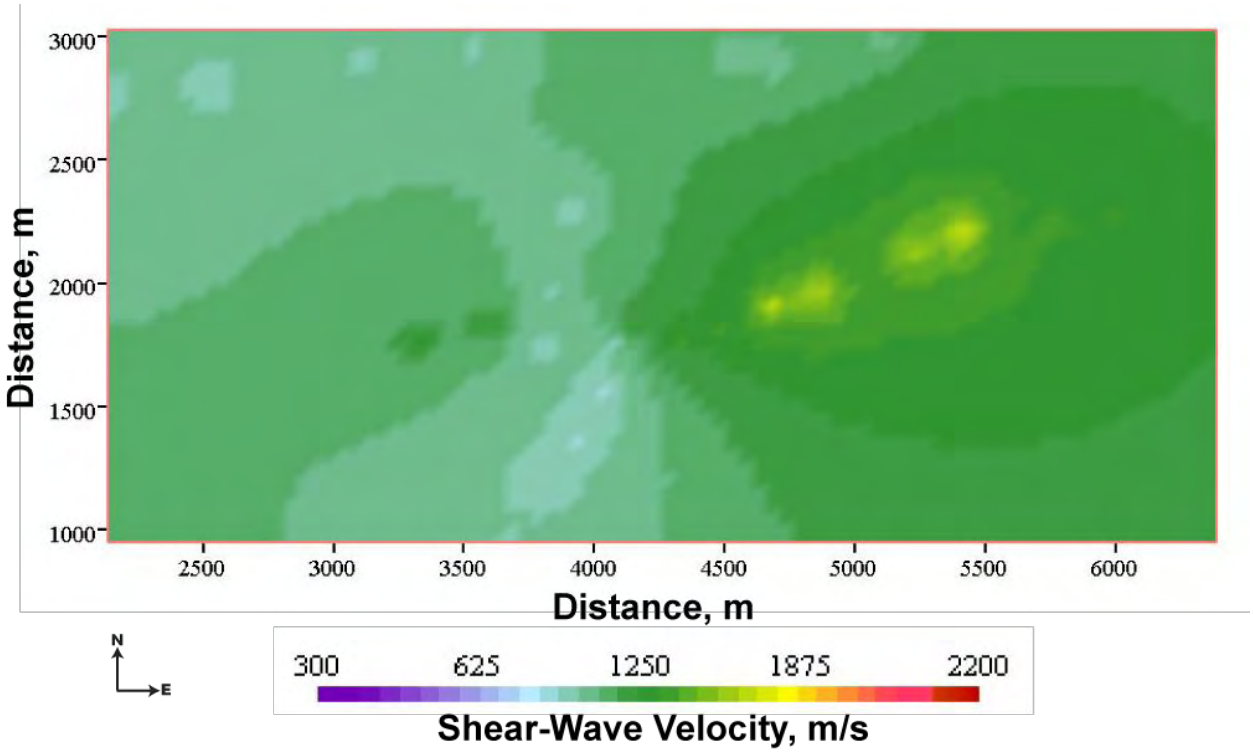

Appendix 1.7: Slice through 3D shear-wave velocity representation at 150 m depth.

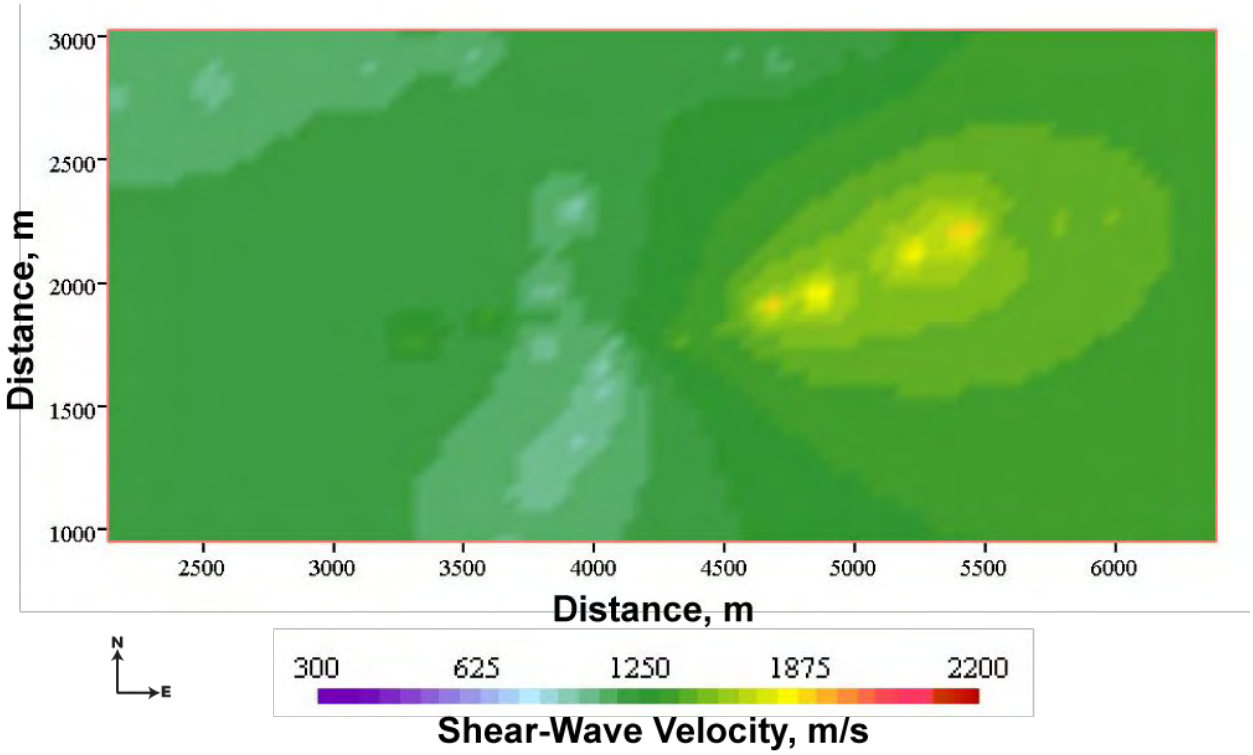

Appendix 1.8: Slice through 3D shear-wave velocity representation at 175 m depth.

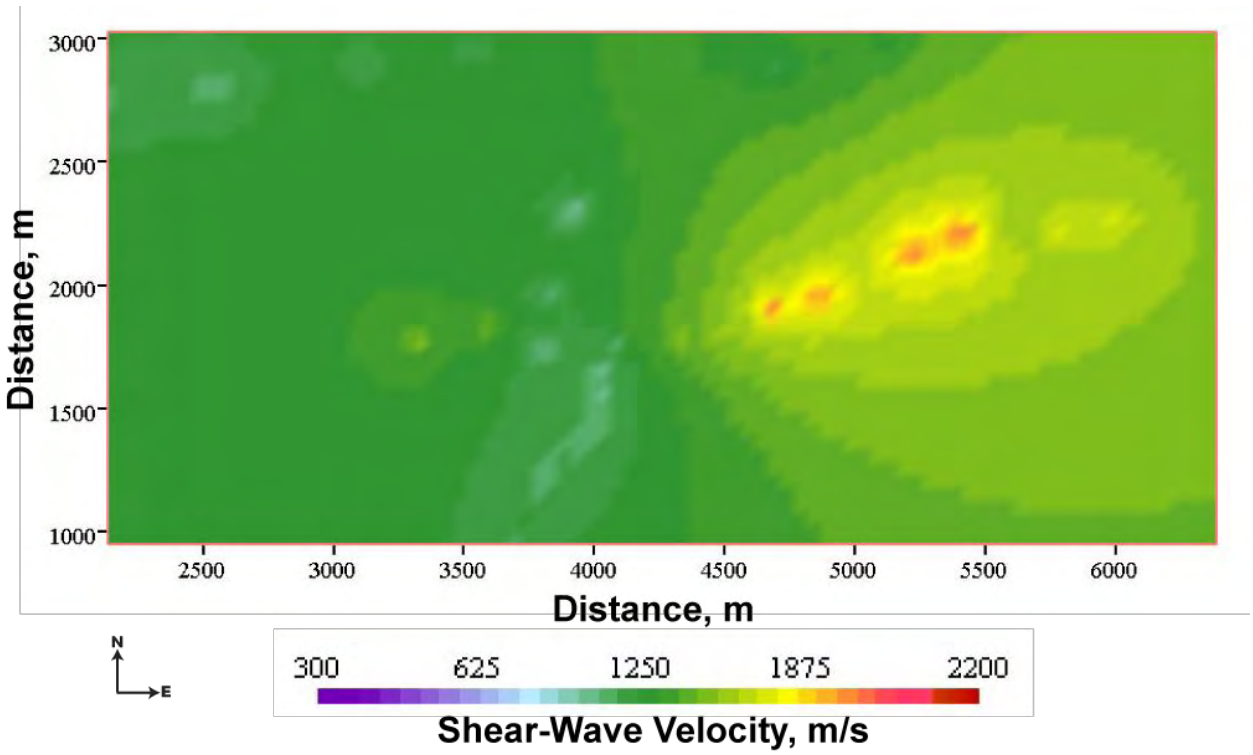

Appendix 1.9: Slice through 3D shear-wave velocity representation at 200 m depth.

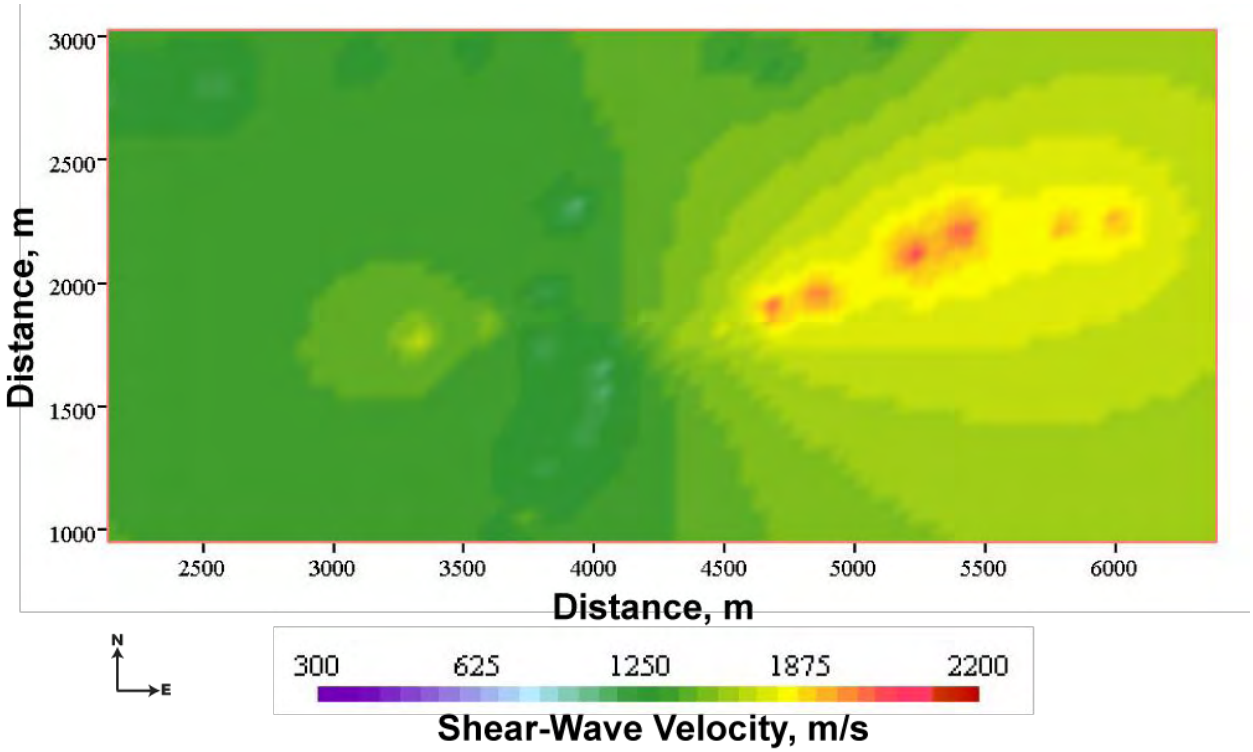

Appendix 1.10: Slice through 3D shear-wave velocity representation at 225 m depth.

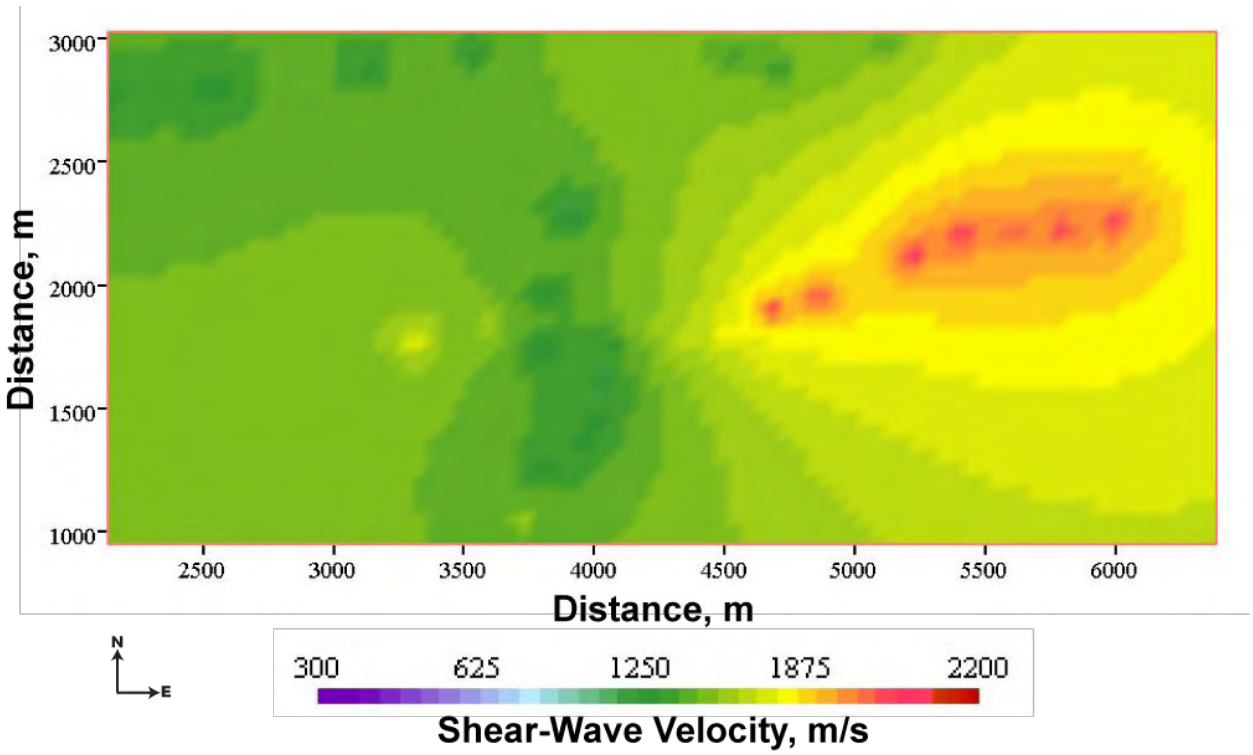

Appendix 1.11: Slice through 3D shear-wave velocity representation at 250 m depth.

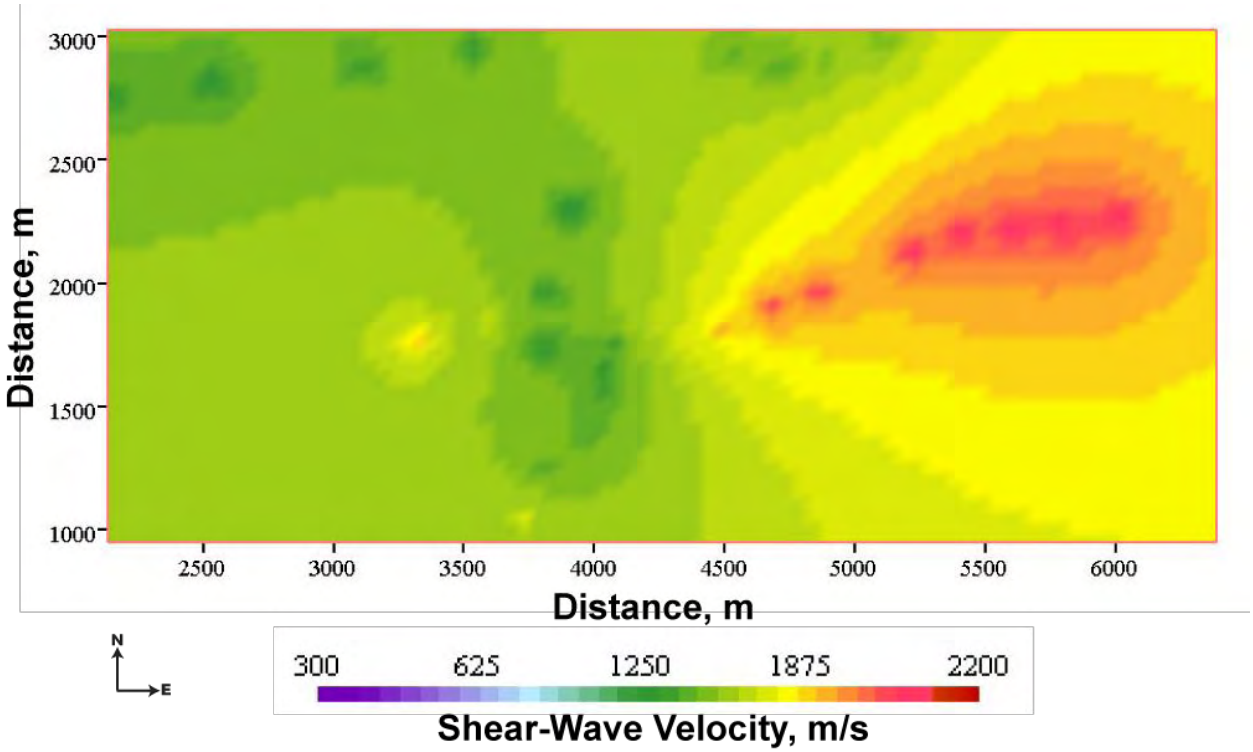

Appendix 1.12: Slice through 3D shear-wave velocity representation at 275 m depth.

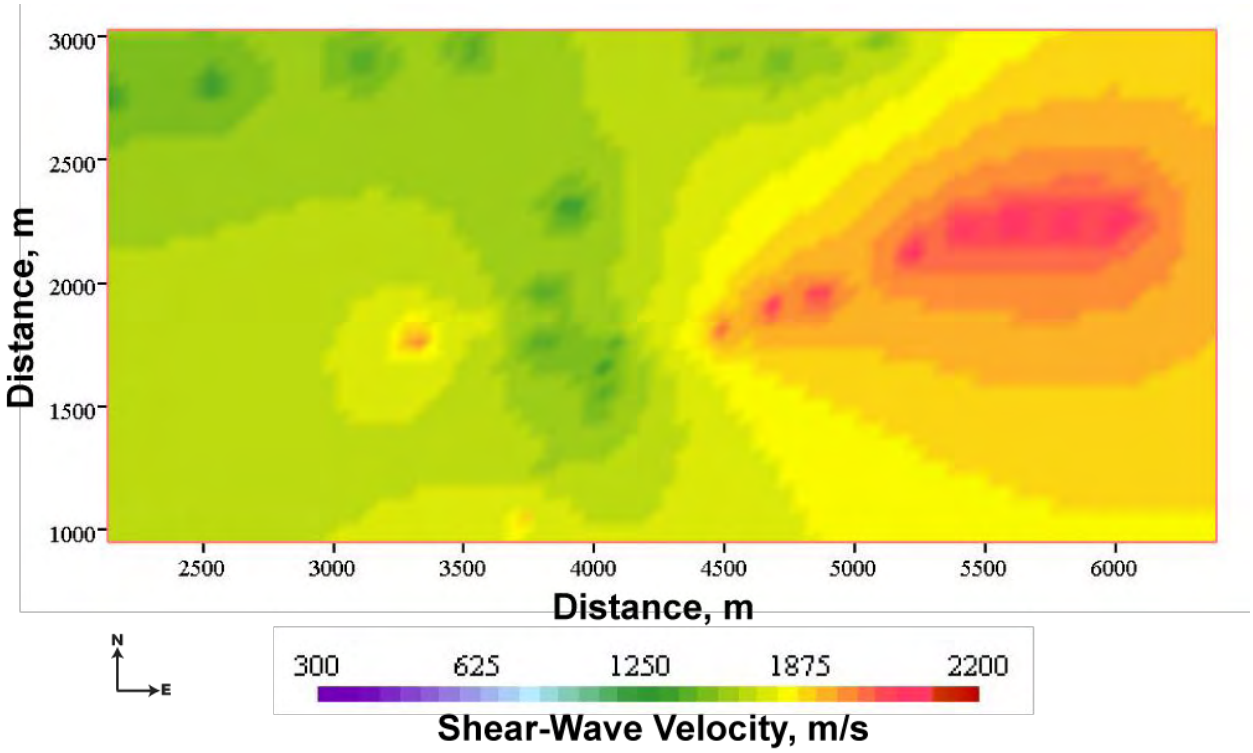

Appendix 1.13: Slice through 3D shear-wave velocity representation at 300 m depth.

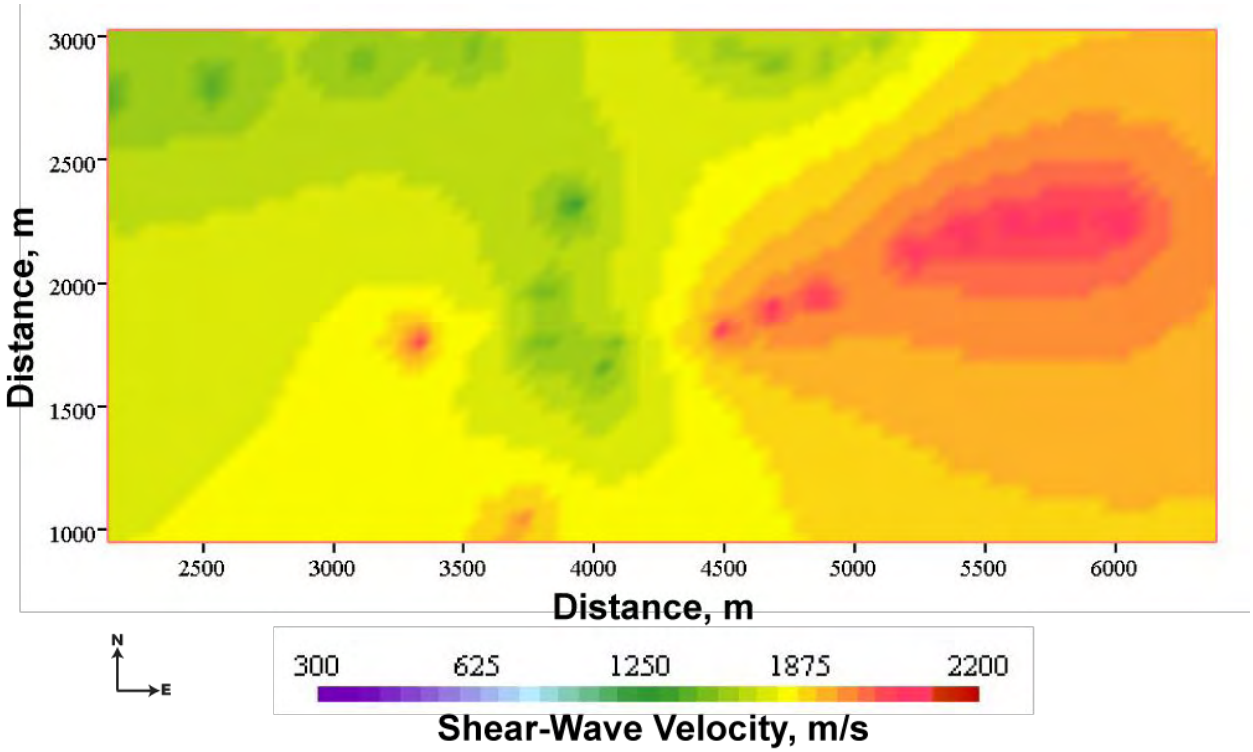

Appendix 1.14: Slice through 3D shear-wave velocity representation at 325 m depth.

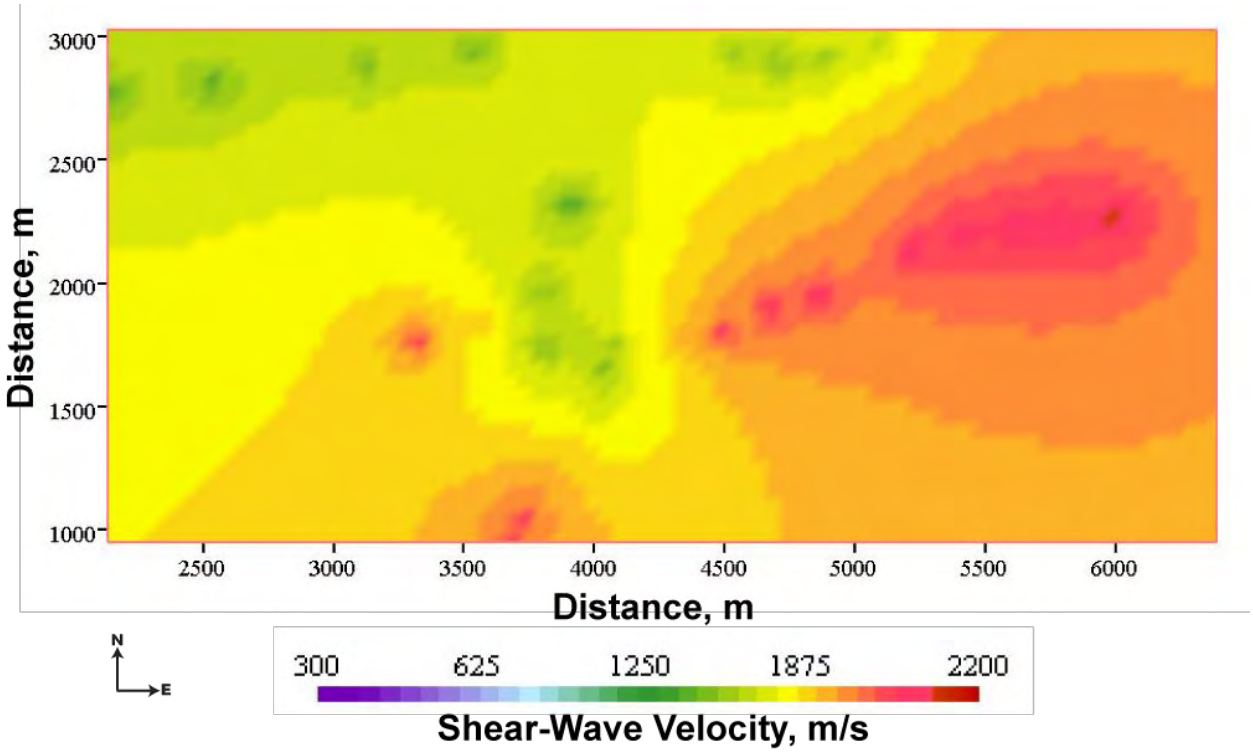

Appendix 1.15: Slice through 3D shear-wave velocity representation at 350 m depth.

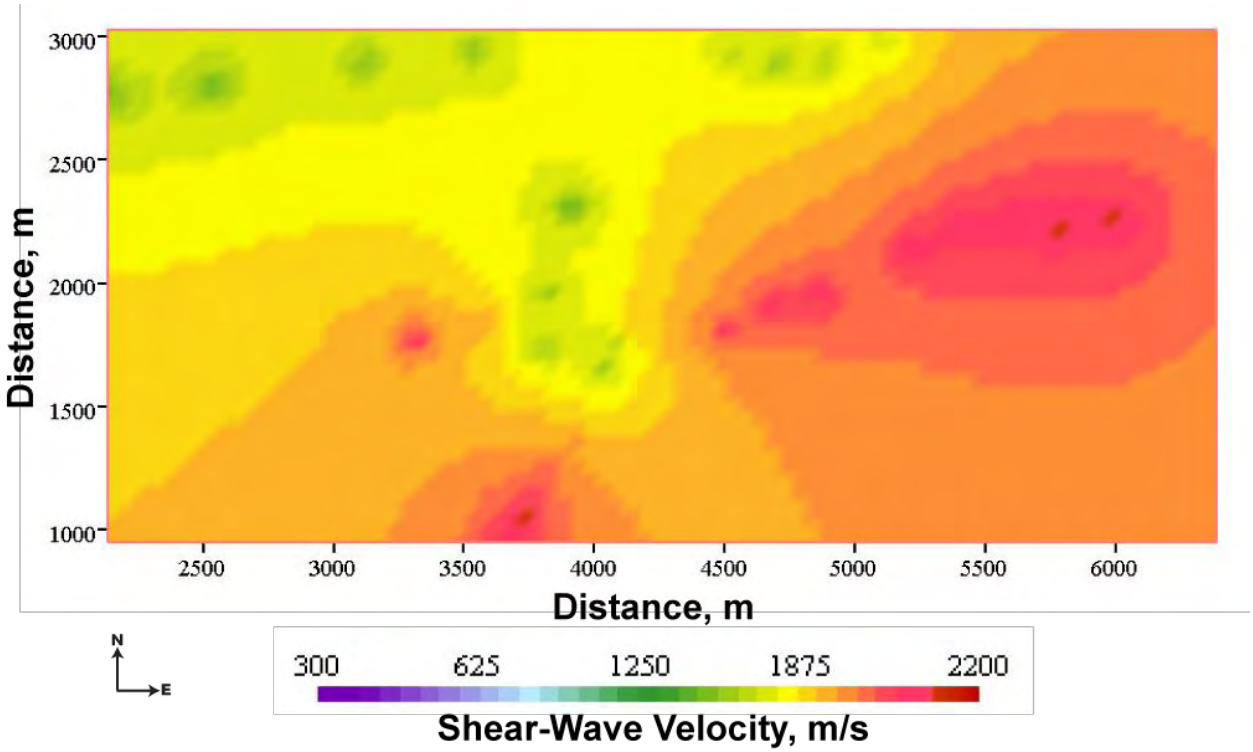

Appendix 1.16: Slice through 3D shear-wave velocity representation at 375 m depth.

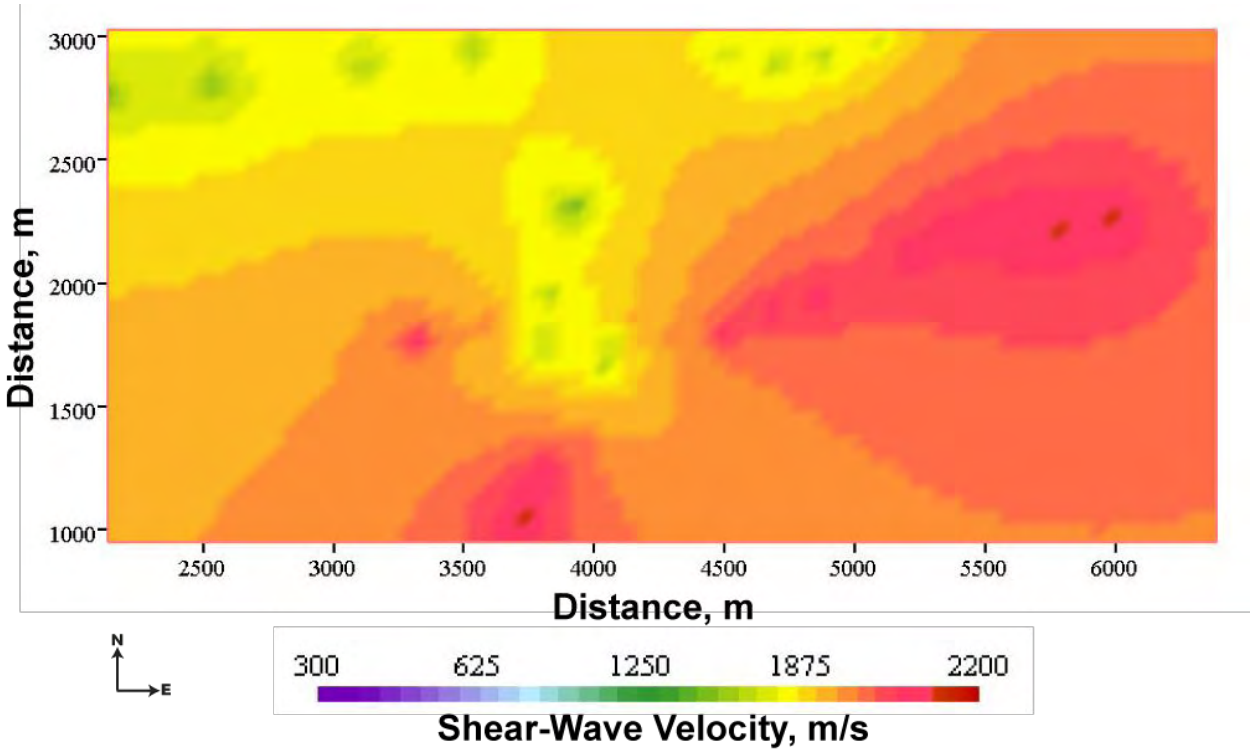

Appendix 1.17: Slice through 3D shear-wave velocity representation at 400 m depth.

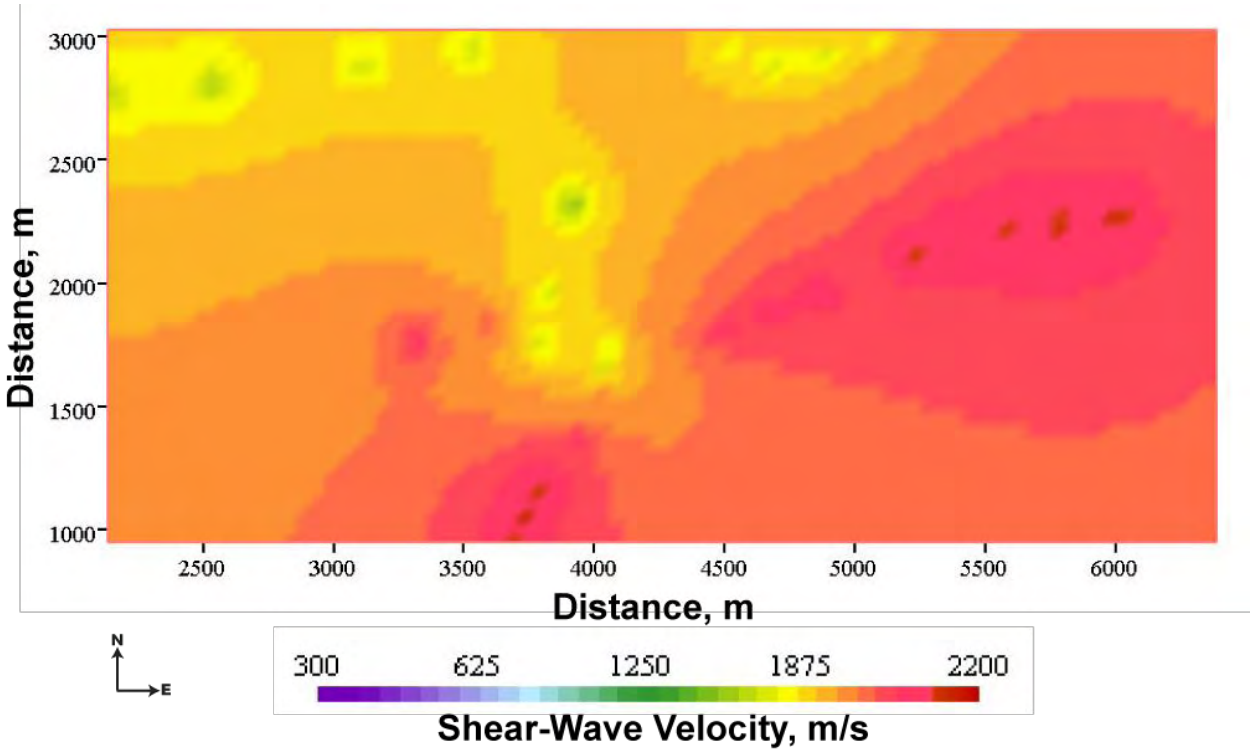

Appendix 1.18: Slice through 3D shear-wave velocity representation at 425 m depth.

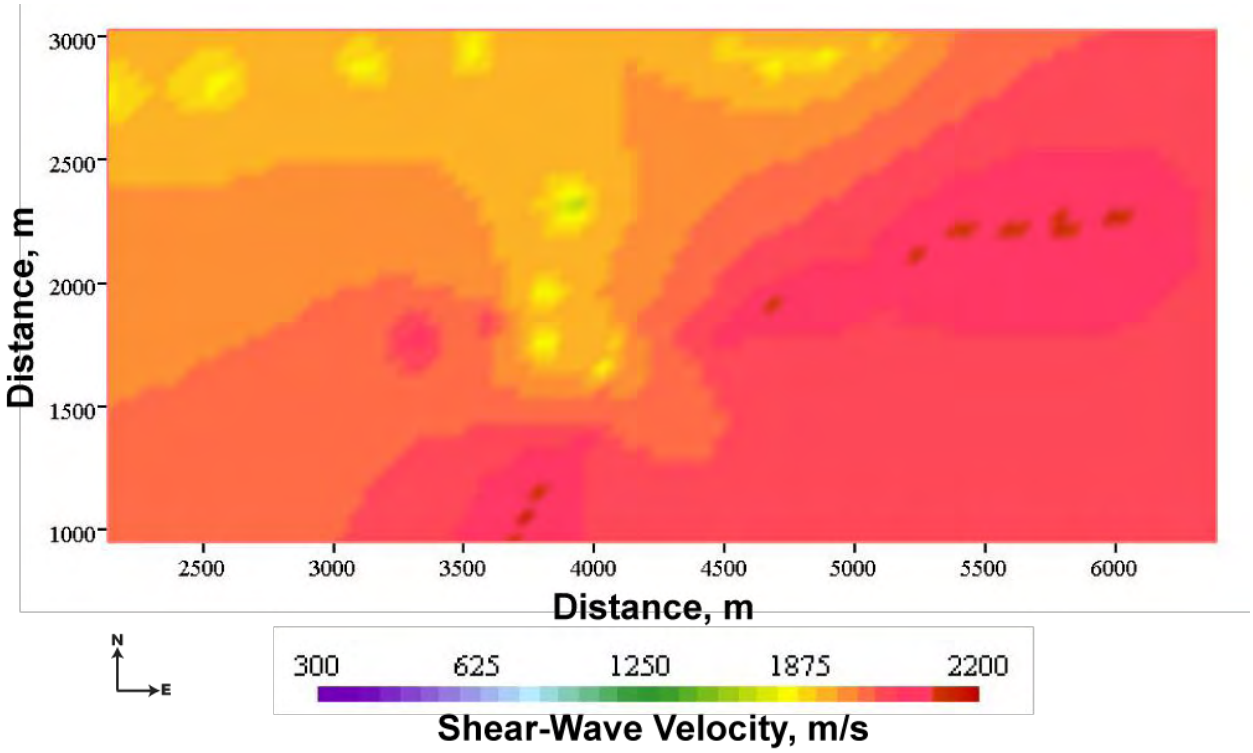

Appendix 1.19: Slice through 3D shear-wave velocity representation at 450 m depth.

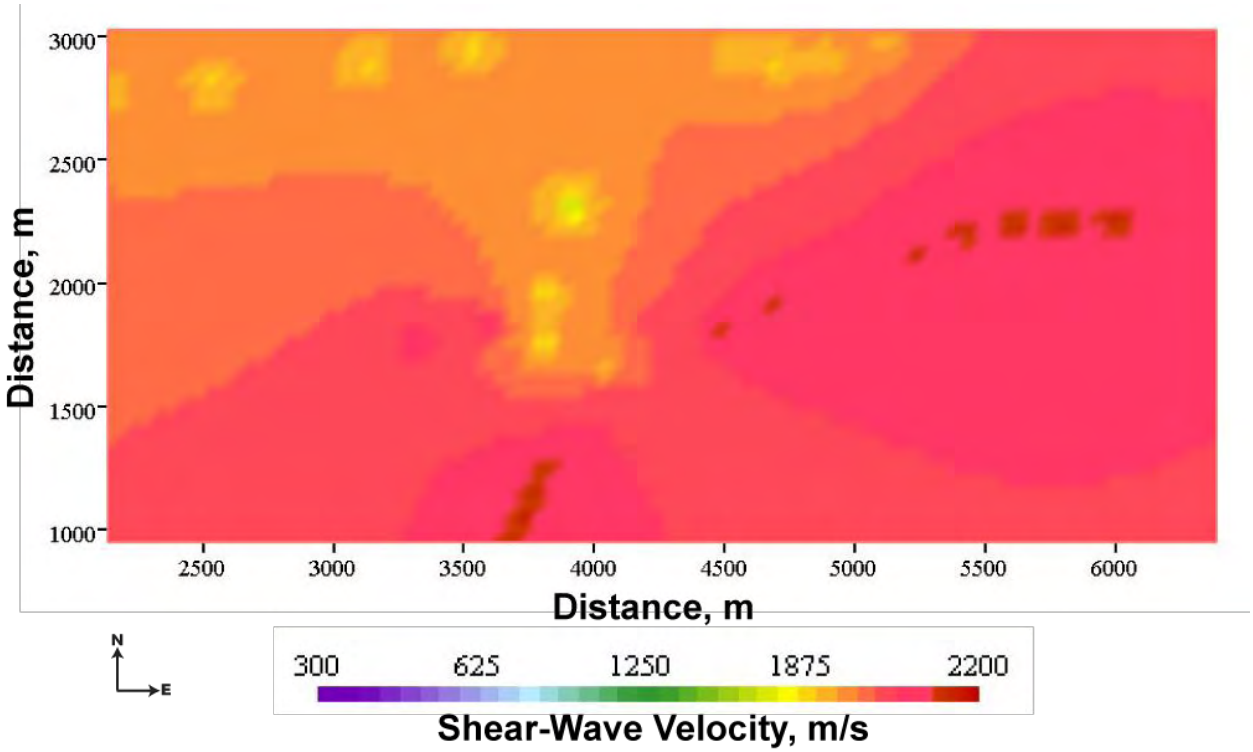

Appendix 1.20: Slice through 3D shear-wave velocity representation at 475 m depth.

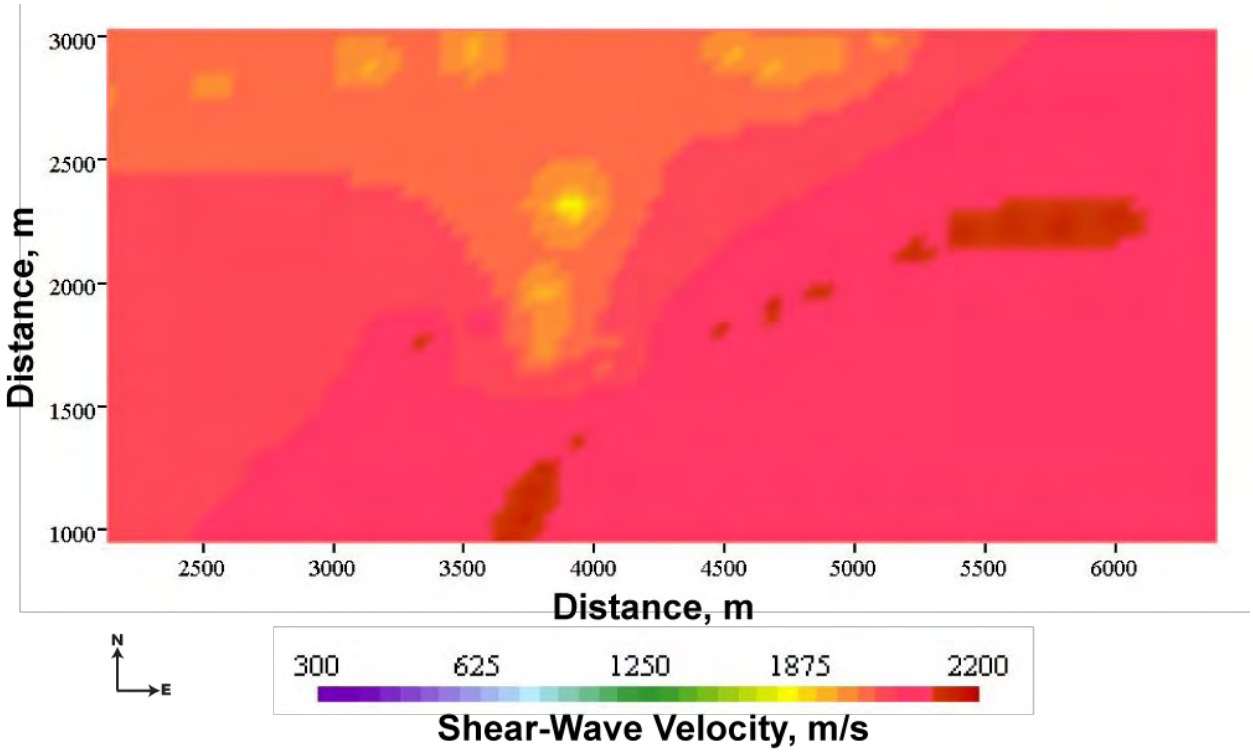

Appendix 1.21: Slice through 3D shear-wave velocity representation at 500 m depth.

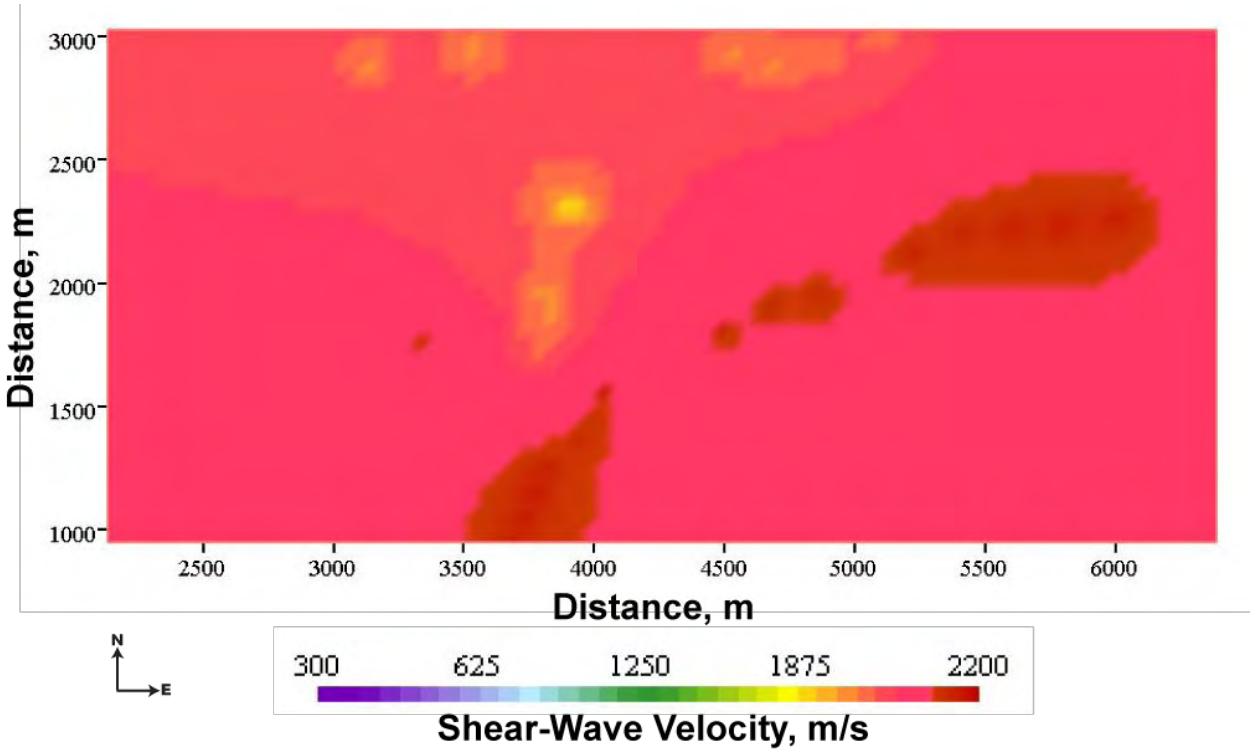

Appendix 1.22: Slice through 3D shear-wave velocity representation at 525 m depth.

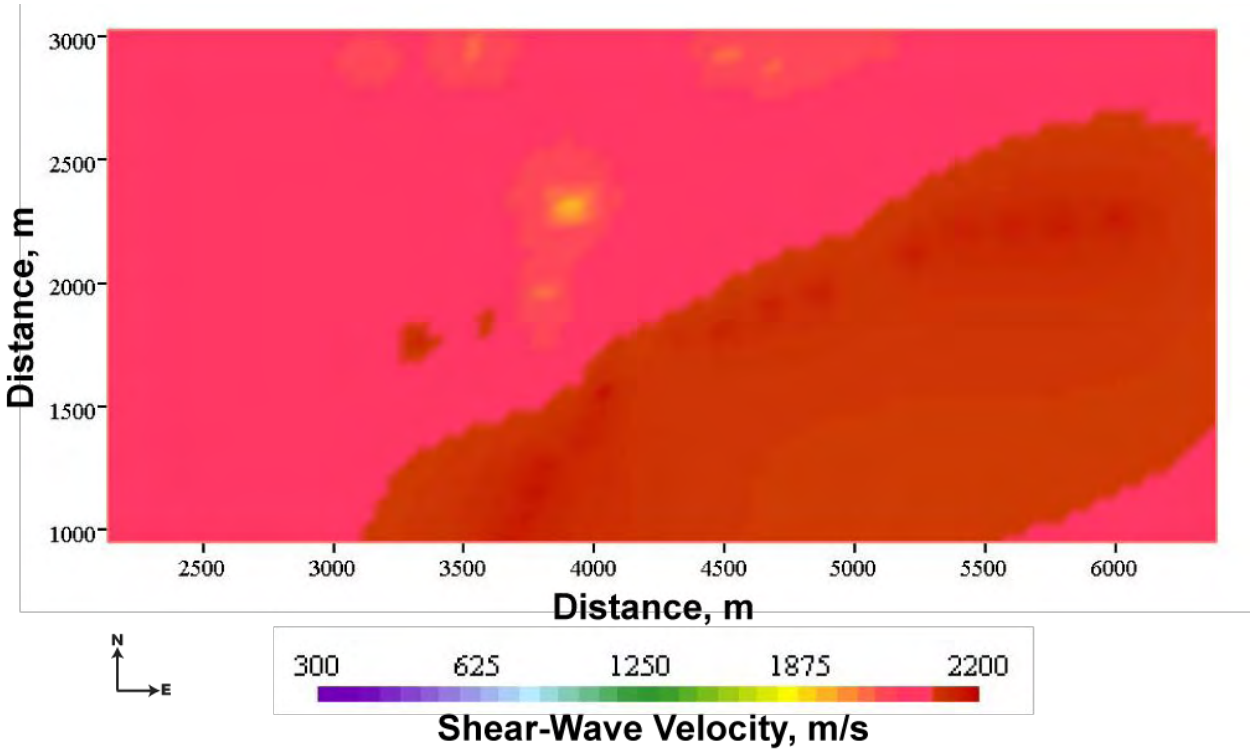

Appendix 1.23: Slice through 3D shear-wave velocity representation at 550 m depth.

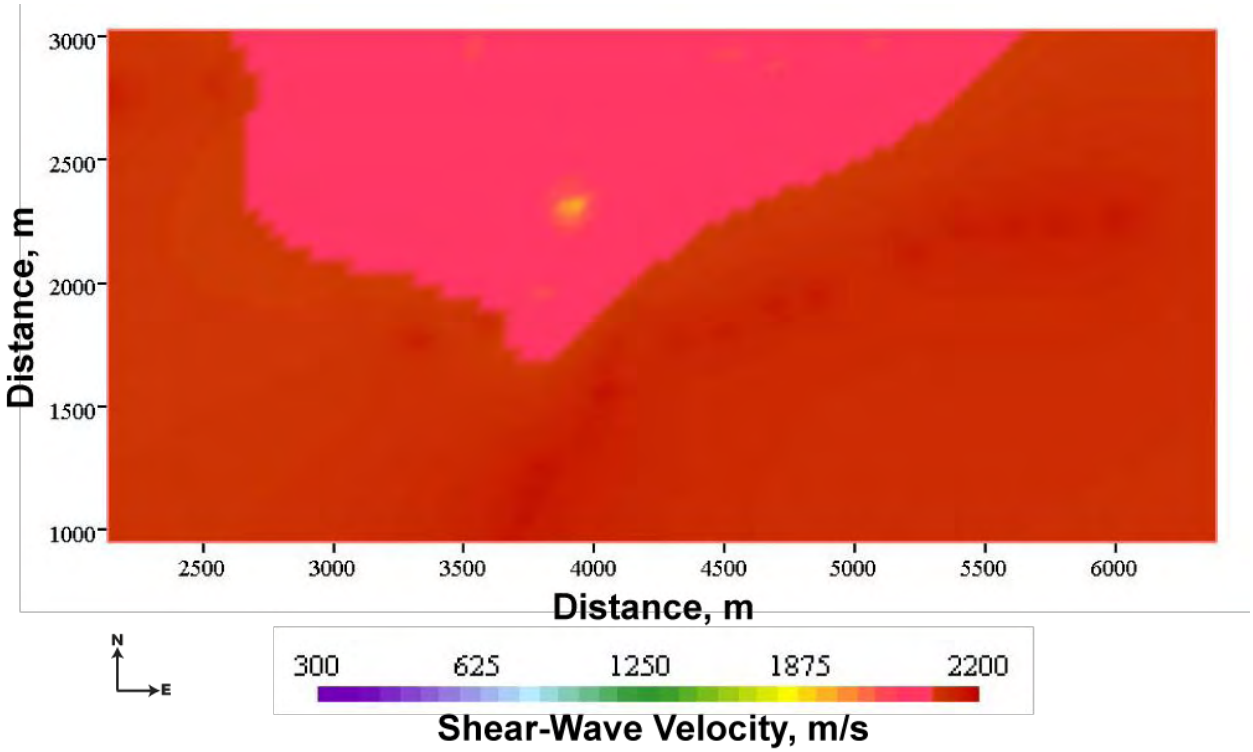

Appendix 1.24: Slice through 3D shear-wave velocity representation at 575 m depth.

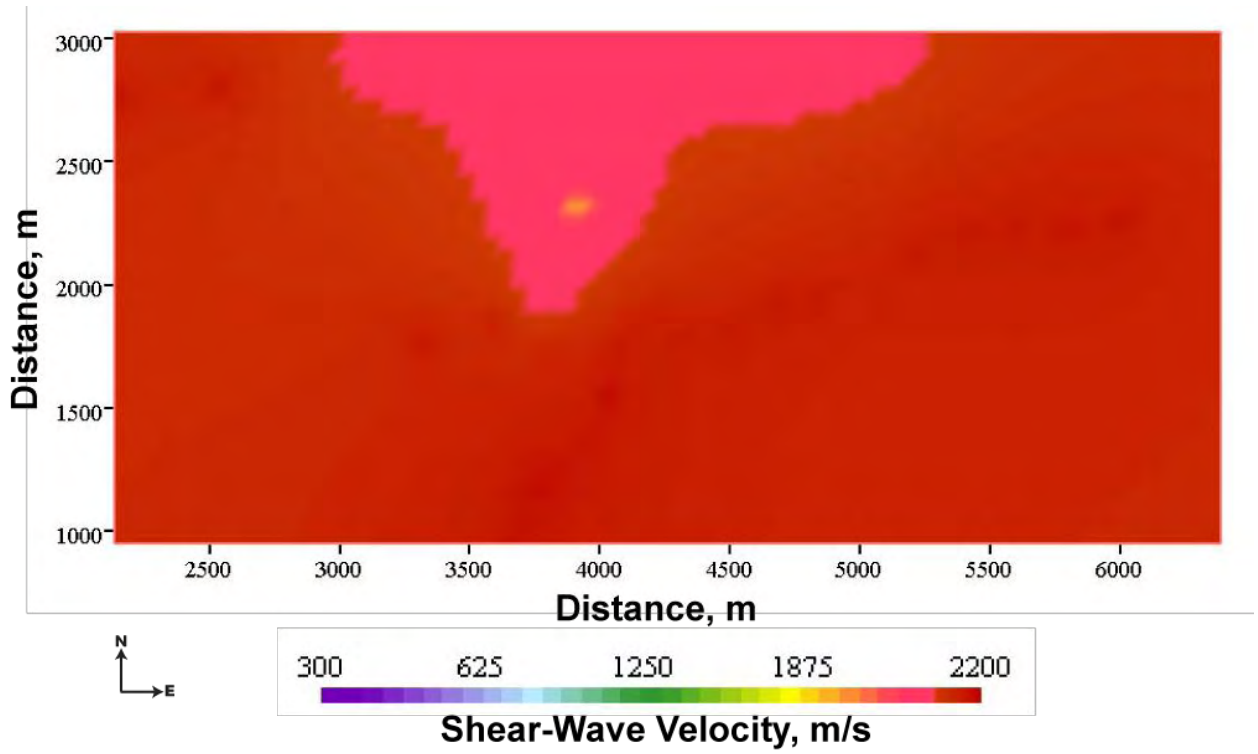

Appendix 1.25: Slice through 3D shear-wave velocity representation at 600 m depth.

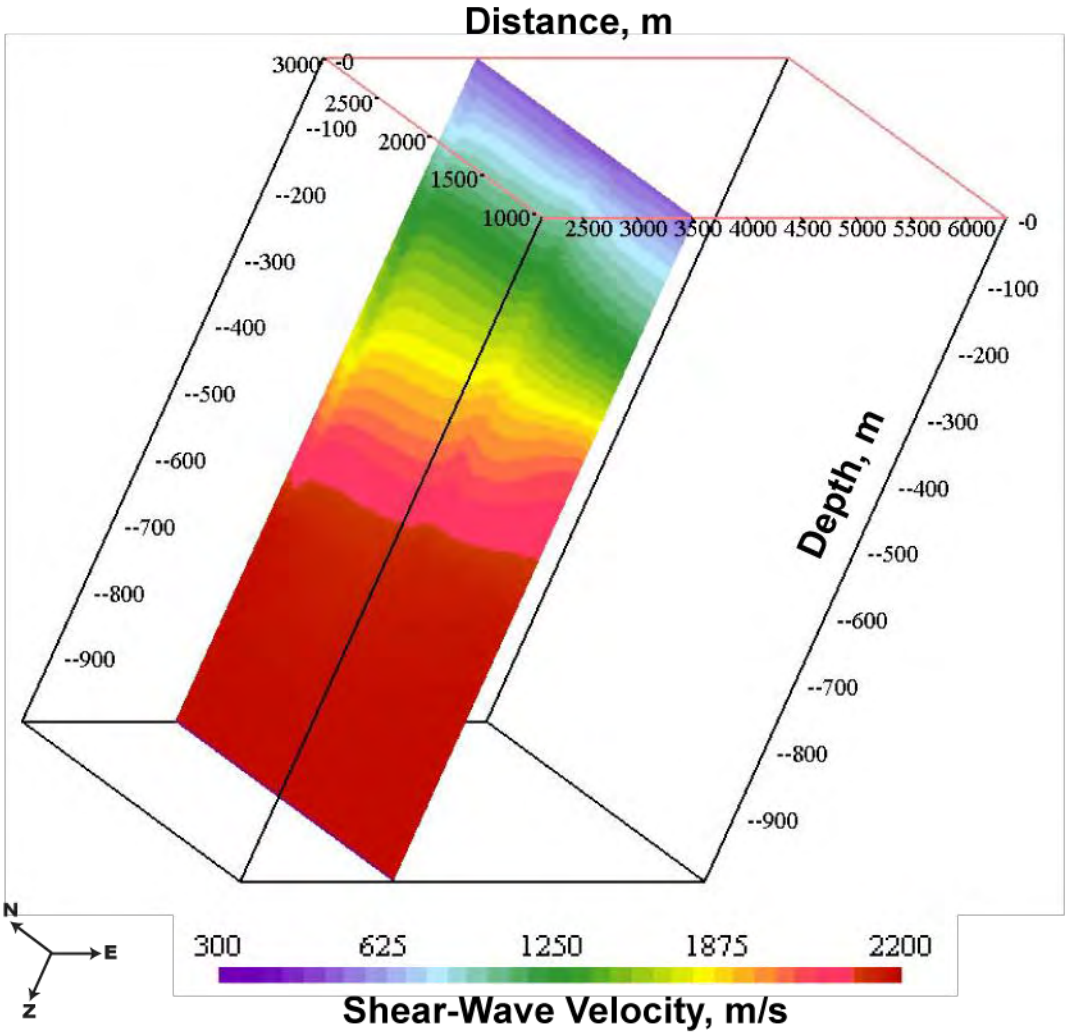

Appendix 2.1: Slice through 3D shear-wave velocity representation at X=3536 m.

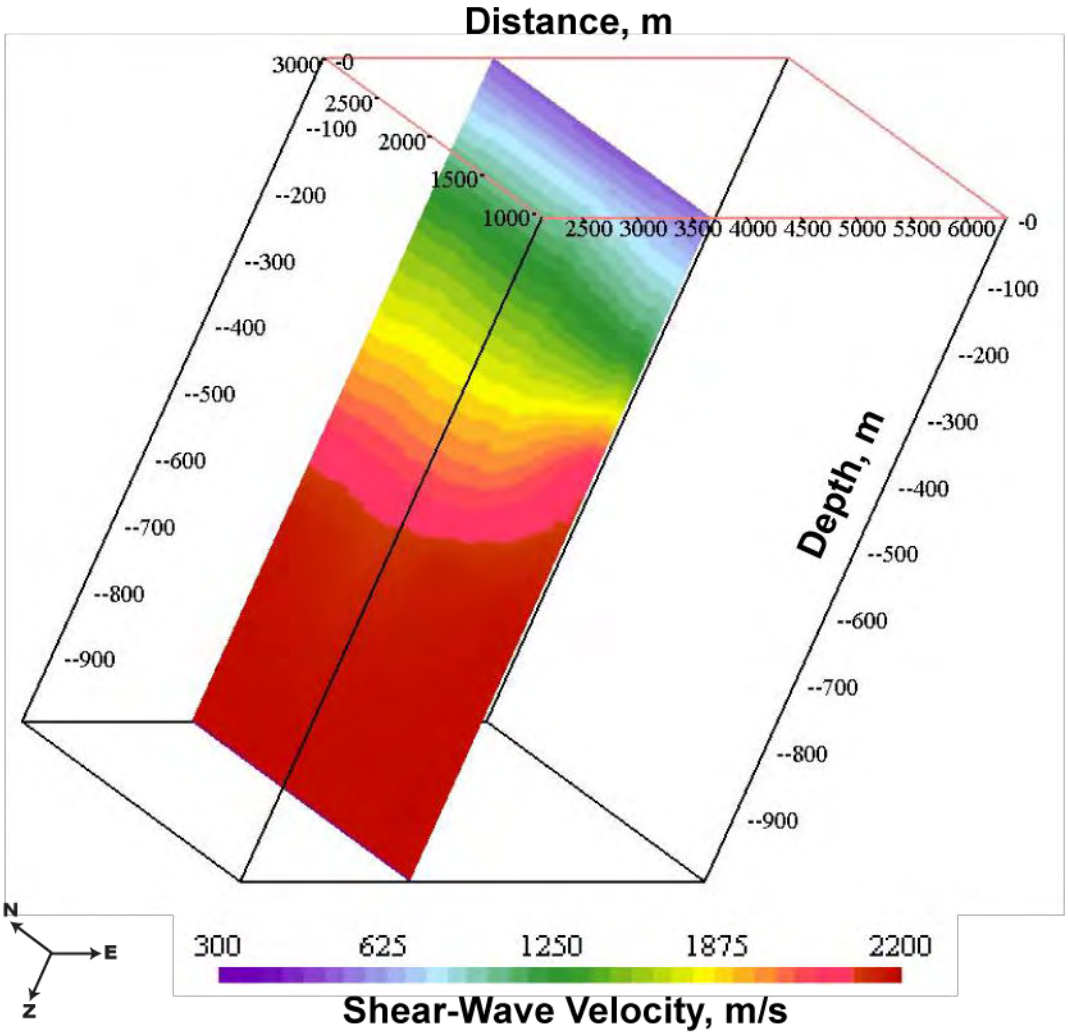

Appendix 2.2: Slice through 3D shear-wave velocity representation at X=3686 m.

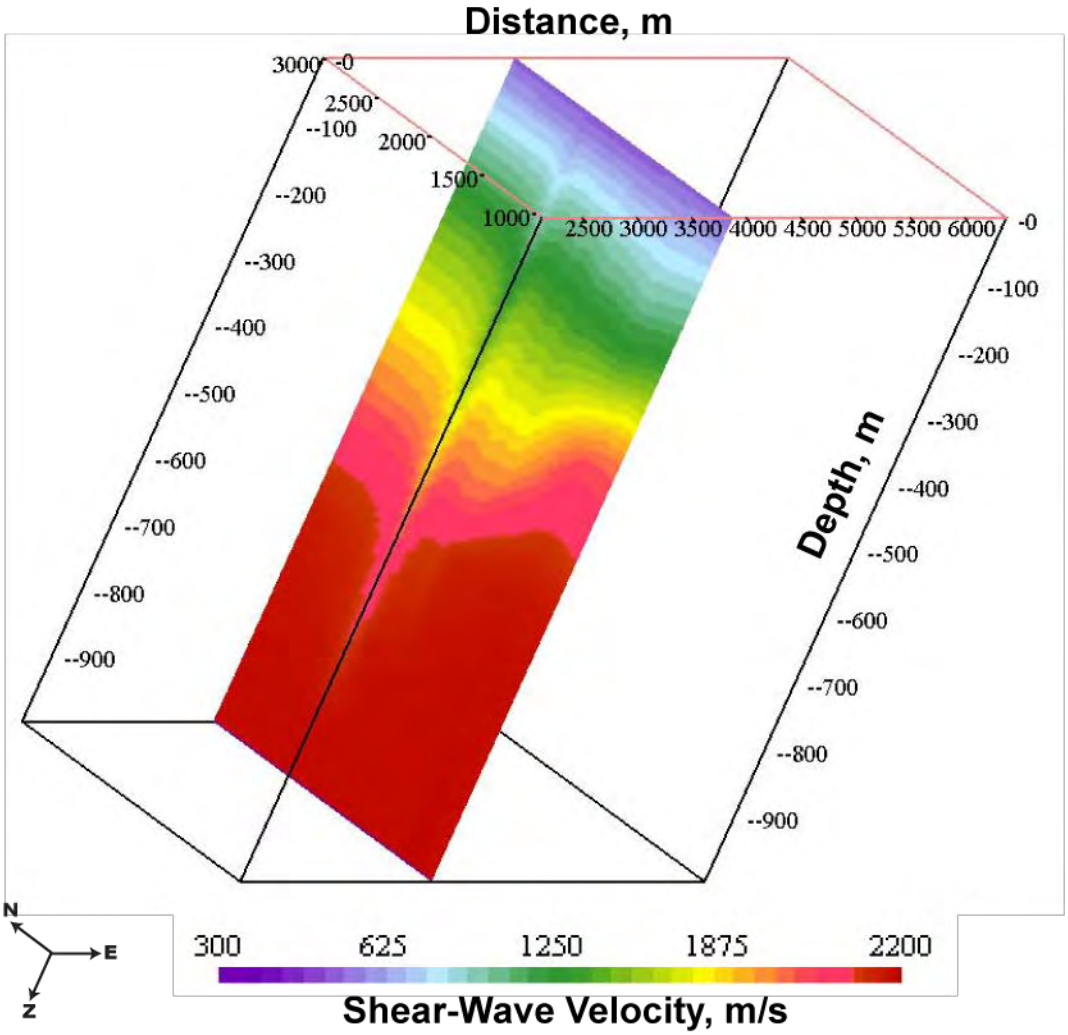

Appendix 2.3: Slice through 3D shear-wave velocity representation at X=3886 m.

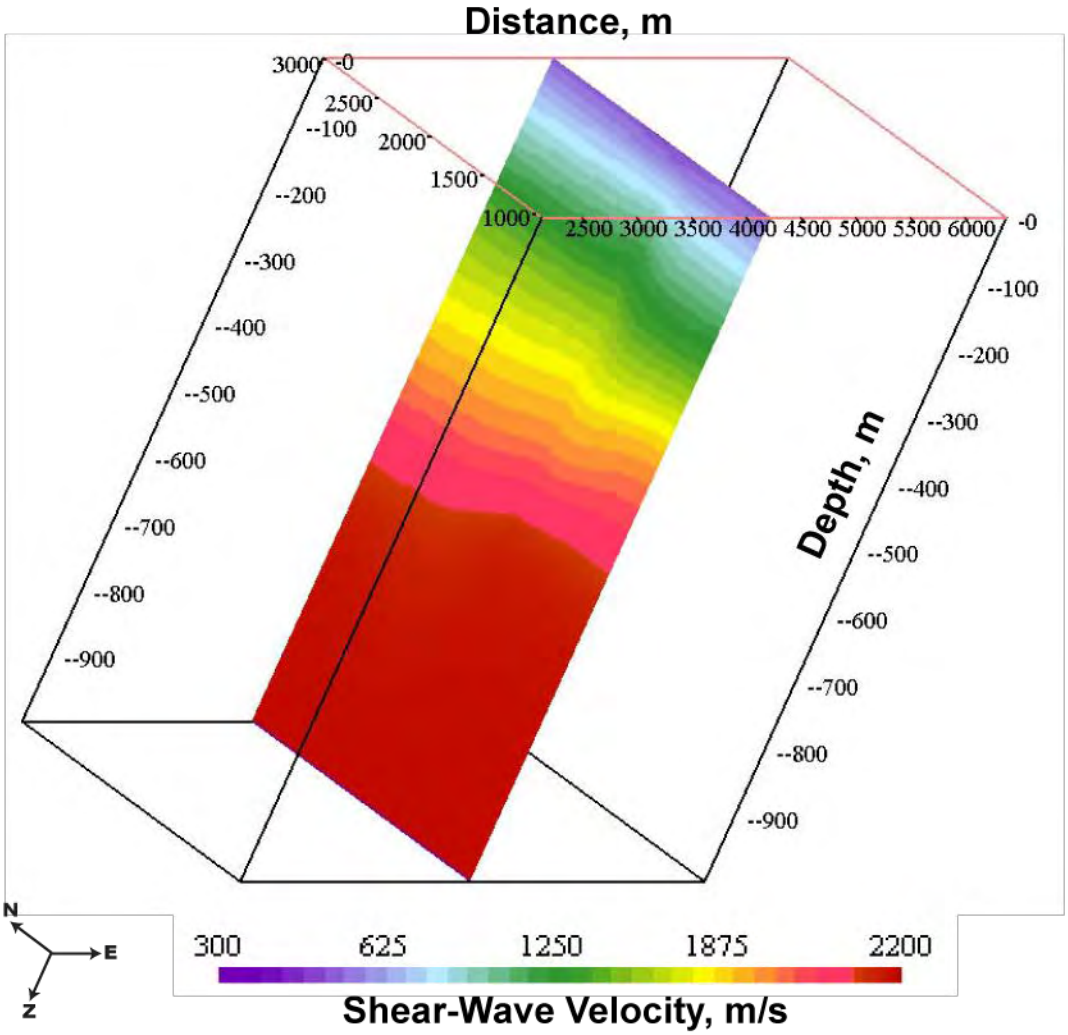

Appendix 2.4: Slice through 3D shear-wave velocity representation at X=4236 m.

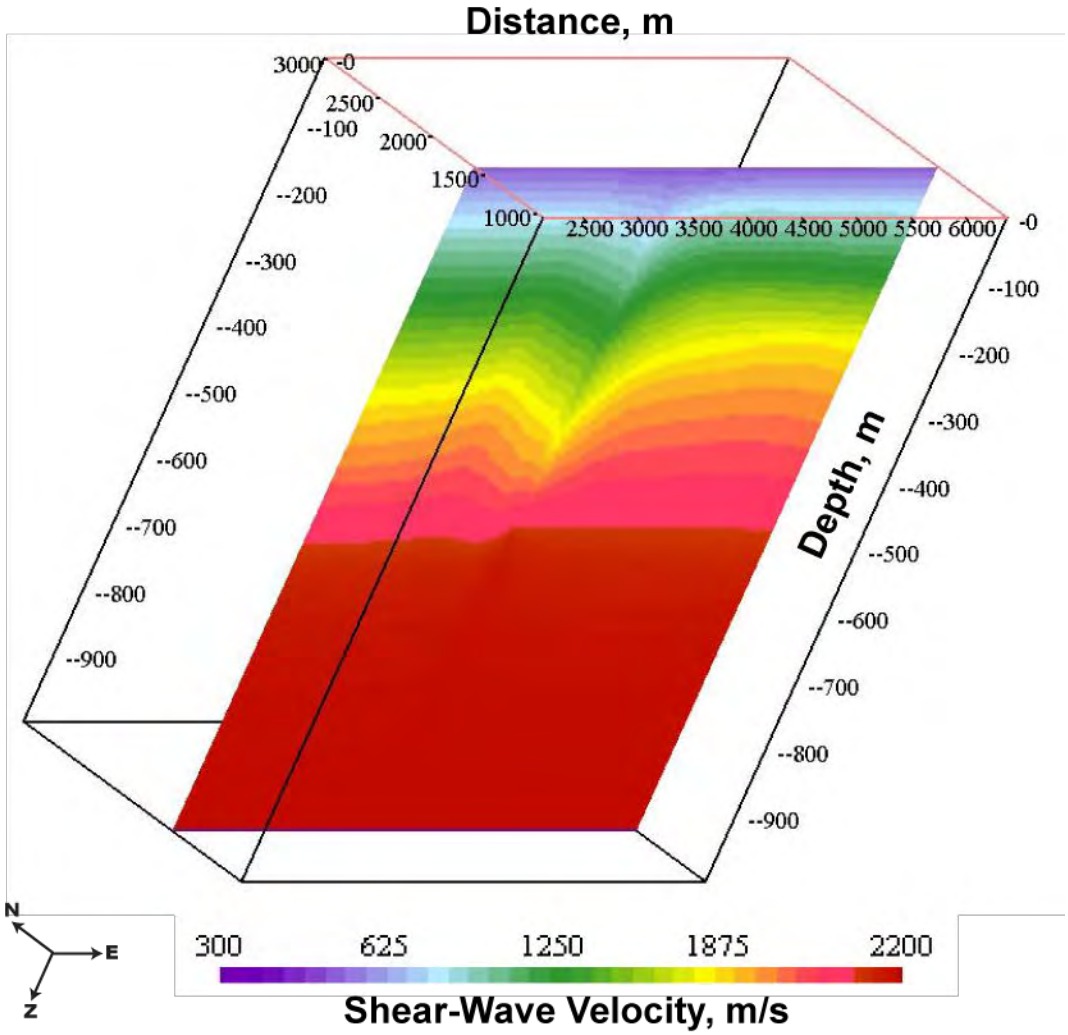

Appendix 3.1: Slice through 3D shear-wave velocity representation at Y=1608 m.

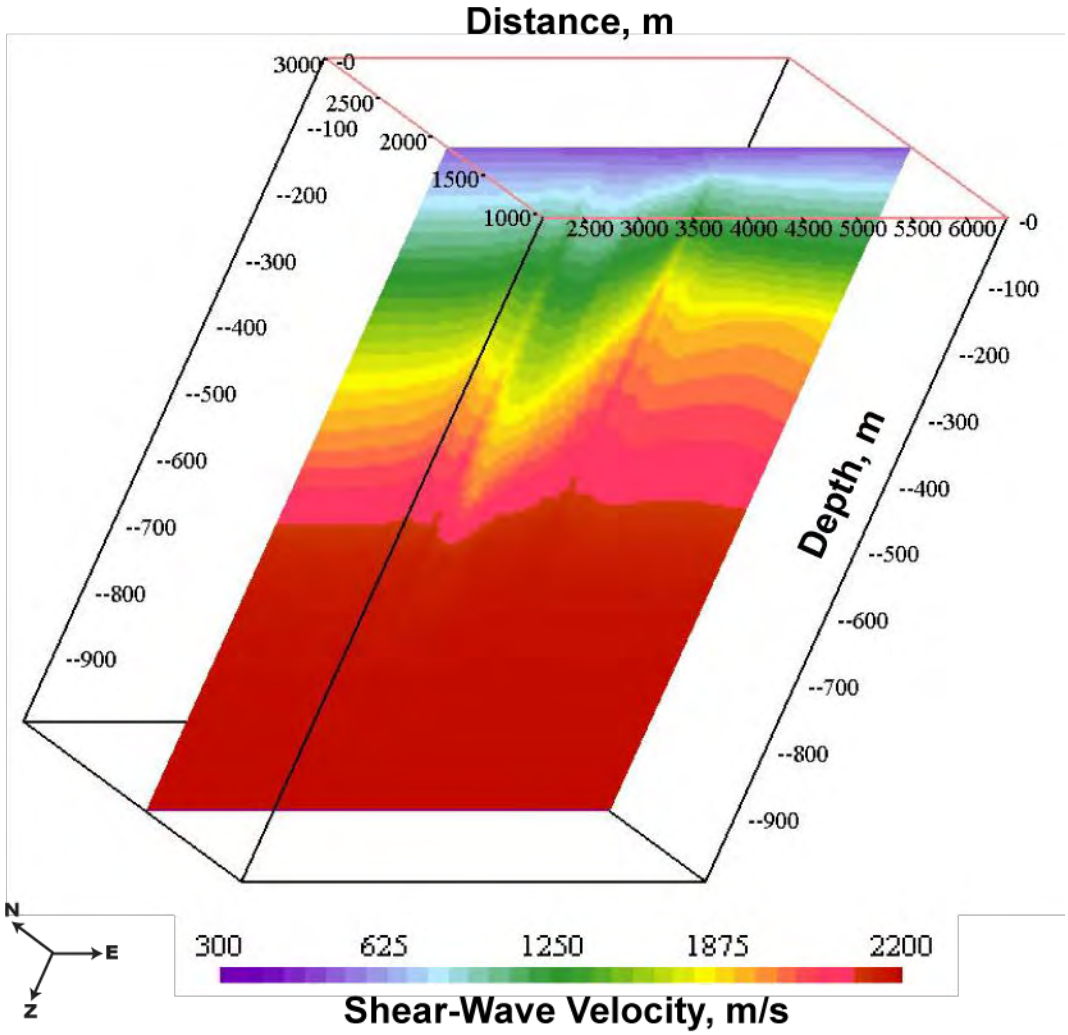

Appendix 3.2: Slice through 3D shear-wave velocity representation at Y=1861 m.

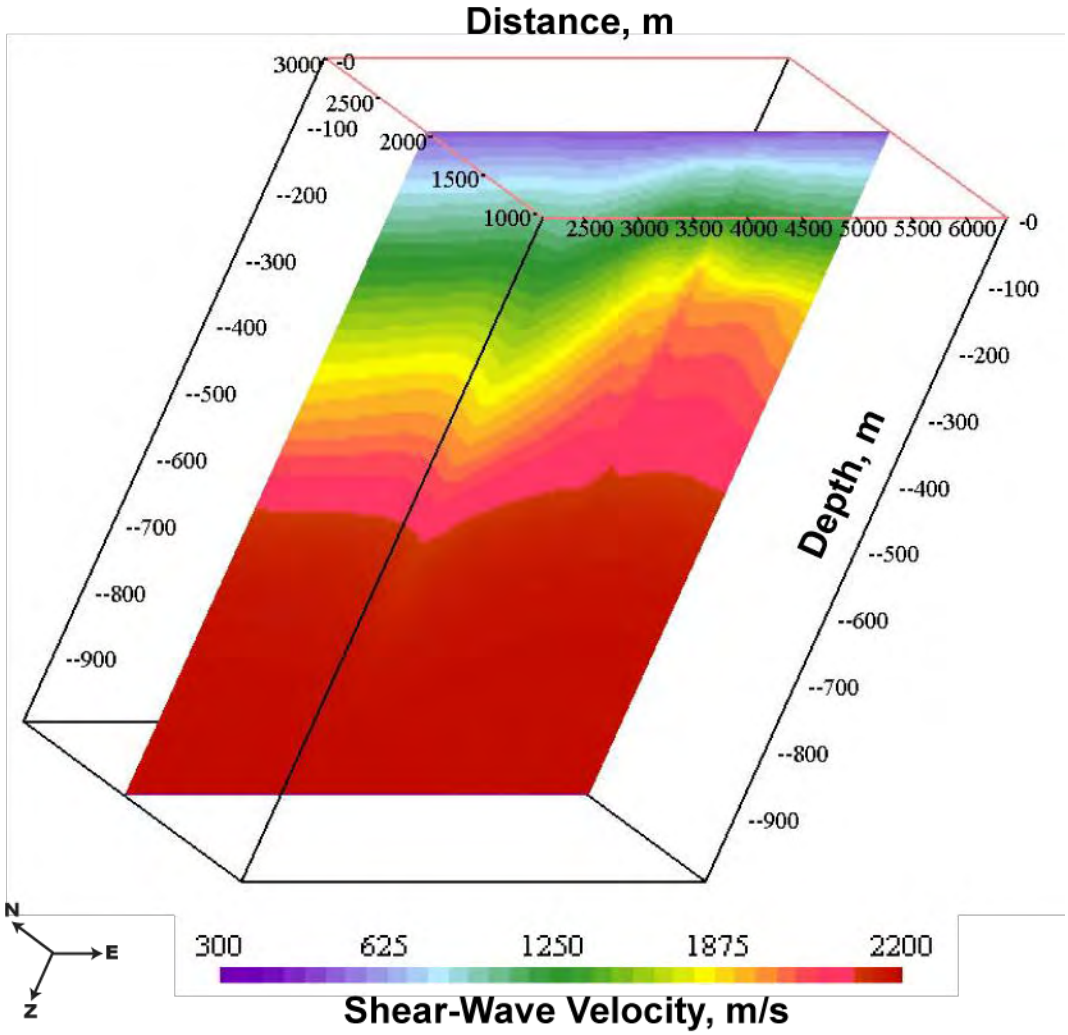

Appendix 3.3: Slice through 3D shear-wave velocity representation at Y=2064 m.

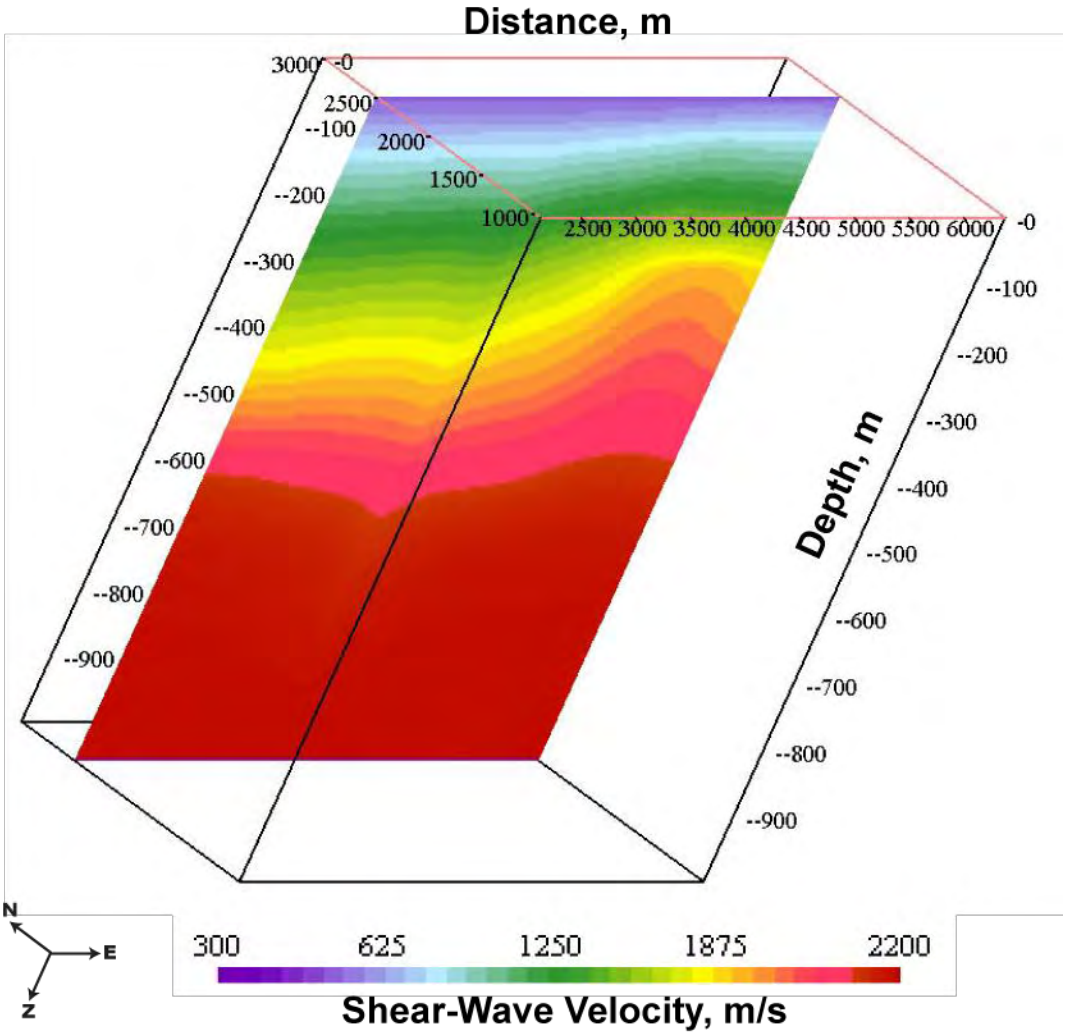

Appendix 3.4: Slice through 3D shear-wave velocity representation at Y=2520 m.

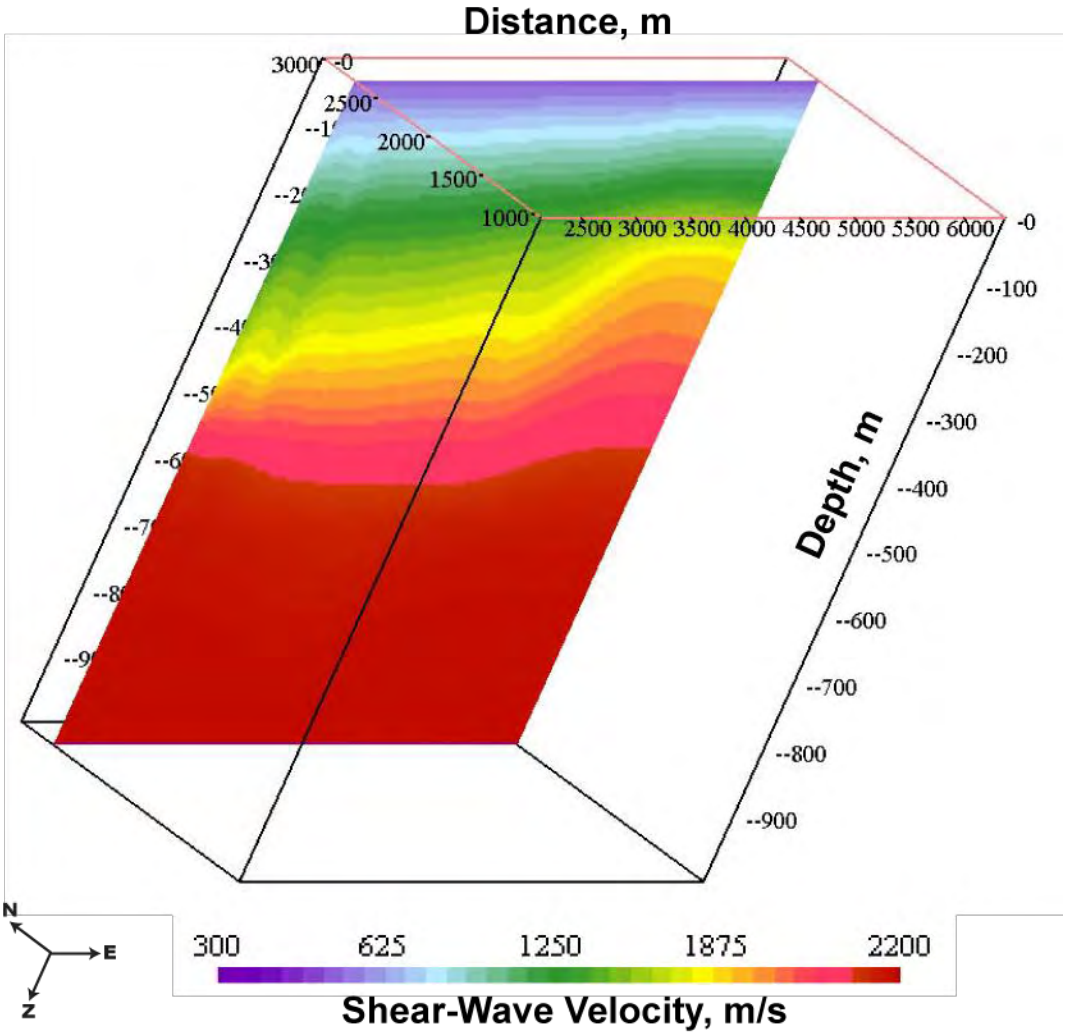

Appendix 3.5: Slice through 3D shear-wave velocity representation at Y=2722 m.